



Surface and bulk nanostructuring of insulators by ultrashort laser pulses

**TZVETA Apostolova
INSTITUTE FOR NUCLEAR RESEARCH AND NUCLEAR ENERGY**

**04/05/2017
Final Report**

DISTRIBUTION A: Distribution approved for public release.

**Air Force Research Laboratory
AF Office Of Scientific Research (AFOSR)/ IOE
Arlington, Virginia 22203
Air Force Materiel Command**

REPORT DOCUMENTATION PAGE				<i>Form Approved</i> OMB No. 0704-0188	
<p>The public reporting burden for this collection of information is estimated to average 1 hour per response, including the time for reviewing instructions, searching existing data sources, gathering and maintaining the data needed, and completing and reviewing the collection of information. Send comments regarding this burden estimate or any other aspect of this collection of information, including suggestions for reducing the burden, to Department of Defense, Executive Services, Directorate (0704-0188). Respondents should be aware that notwithstanding any other provision of law, no person shall be subject to any penalty for failing to comply with a collection of information if it does not display a currently valid OMB control number.</p> <p>PLEASE DO NOT RETURN YOUR FORM TO THE ABOVE ORGANIZATION.</p>					
1. REPORT DATE (DD-MM-YYYY) 05-04-2017		2. REPORT TYPE Final		3. DATES COVERED (From - To) 01 May 2015 to 30 Apr 2016	
4. TITLE AND SUBTITLE Surface and bulk nanostructuring of insulators by ultrashort laser pulses				5a. CONTRACT NUMBER	
				5b. GRANT NUMBER FA9550-15-1-0197	
				5c. PROGRAM ELEMENT NUMBER 61102F	
6. AUTHOR(S) TZVETA Apostolova				5d. PROJECT NUMBER	
				5e. TASK NUMBER	
				5f. WORK UNIT NUMBER	
7. PERFORMING ORGANIZATION NAME(S) AND ADDRESS(ES) INSTITUTE FOR NUCLEAR RESEARCH AND NUCLEAR ENERGY Mladost Distr., 72 SOFIA, 1784 BG				8. PERFORMING ORGANIZATION REPORT NUMBER	
9. SPONSORING/MONITORING AGENCY NAME(S) AND ADDRESS(ES) EOARD Unit 4515 APO AE 09421-4515				10. SPONSOR/MONITOR'S ACRONYM(S) AFRL/AFOSR IOE	
				11. SPONSOR/MONITOR'S REPORT NUMBER(S) AFRL-AFOSR-UK-TR-2017-0025	
12. DISTRIBUTION/AVAILABILITY STATEMENT A DISTRIBUTION UNLIMITED: PB Public Release					
13. SUPPLEMENTARY NOTES					
14. ABSTRACT The feasibility for femto and attosecond pulse generation from diamond subjected to intense fs laser pulse with mid-infrared wavelength was explored by further investigating the non-perturbative scaling of the generated harmonics with the laser field and their bandstructure dependence since recent experimental and theoretical investigations in the literature show that high harmonic generation HHG in wide band-gap semiconductors (insulators) may lead to brighter sources due to the high laser induced carrier density and ability to withstand the driving laser fields necessary for inducing strong nonlinear and non perturbative effects leading to HHG.					
15. SUBJECT TERMS Nanostructuring of bulk insulators, sub-picosecond electronic and structural events, photo-excitation and relaxation of carriers, carrier-lattice interactions, EOARD					
16. SECURITY CLASSIFICATION OF:			17. LIMITATION OF ABSTRACT SAR	18. NUMBER OF PAGES	19a. NAME OF RESPONSIBLE PERSON CUMMINGS, RUSSELL
a. REPORT Unclassified	b. ABSTRACT Unclassified	c. THIS PAGE Unclassified			19b. TELEPHONE NUMBER (Include area code) 011-44-1895-616021

Report on proposal FA9550-15-1-0197

**”Surface and bulk nanostructuring of insulators by ultrashort
laser pulses”**

Principal Investigator Tzveta Apostolova

Period of Performance 01 May 2015 to 30 March 2017

CONTENTS

List of Figures	3
I. Summary	4
II. Photoionization of monocrystalline CVD diamond irradiated with ultrashort intense laser pulse	4
A. Introduction	4
B. Methods, Assumptions and Procedures	5
C. Results and Discussion	7
D. Conclusion	12
III. Ultrafast photoionization and excitation of surface-plasmon-polaritons on diamond surfaces	13
A. Introduction	13
B. Methods, Assumptions and Procedures	15
C. Results and Discussion	19
D. Conclusion	21
IV. High harmonic generation from bulk diamond driven by intense femtosecond laser pulse	21
A. Introduction	21
B. Methods, Assumptions and Procedures	23
C. Results and Discussion	24
D. Conclusion	27
References	27

LIST OF FIGURES

1	Static band structure of diamond	32
2	Time-evolution of the electron density	32
3	Time-evolution of the macroscopic polarization density	33
4	Density of conduction band states after the irradiation of diamond	33
5	Intensity dependence of the photoionization yield	34
6	Perturbative vs. non-perturbative multiphoton ionization of diamond	35
7	Comparison of theory and data	36
8	Time evolution of the free-electron density in diamond irradiated by 200fs laser pulse	36
9	Excitation energy of electrons interacting with 200fs laser pulse	37
10	Density of conduction states after the irradiation of bulk diamond with 200fs laser pulse	37
11	Time-dependent carrier generation and recombination rates	38
12	Conduction electron density for the two mechanisms	38
13	Frequency dependence of the real and imaginary part of the inverse dielectric function	39
14	2D intensity map of the logarithm of the transient efficacy factor of laser-irradiated diamond	39
15	Transient variation of the efficacy factor	40
16	SEM images	41
17	HHG spectra	41
18	High-energy cutoff	42
19	HHG spectral intensity	42
20	Current density distribution in diamond bulk	43
21	Momentum-dependent HHG spectrum	44
22	Time evolution of the optically-induced polarization current	45
23	Harmonic spectrum for interband, intraband and total currents	46
24	Time-profile of the polarization current generating the 5th harmonic	47

I. SUMMARY

Diamond is a material, exhibiting unique mechanical, thermal and electrical properties, as well as high electron and hole mobility [1], promoting its high performance in microelectronic devices. In this study we have investigated the microscopic processes involved in laser irradiation of diamond and then we have extended it for three different potential applications.

Photoionization of diamond below and close to the graphitization threshold as in the experimental procedure used to write graphitic electrodes inside diamond bulk by laser irradiation [2–4] for the fabrication of three-dimensional (3D) devices was theoretically described and compared to laser-induced current in monocrystalline diamond detector measured by Transient Currents Technique (TCT) in a wide range of laser intensities and at different bias voltages.

In connection to the fact that diamond is a basic ingredient in modern nanophotonics [5, 6] and due to its high refractive index in UV-VIS range, it is prospective material for all-dielectric [7] and hybrid metal-dielectric nano-photonic devices and circuits [8–10] we next have studied the process in which despite its dielectric character, similarly to silicon it can be promptly turned by intense ultrashort laser pulses into short-lived plasmonic state, becoming so-called "virtual plasmonic material", supporting photoexcitation and propagation of surface plasmon-polaritons (SPPs). The potential applications are in ultrafast optical switching, spatial phase modulation and saturable absorption [11–15].

The feasibility for femto and attosecond pulse generation from diamond subjected to intense fs laser pulse with mid-infrared wavelength was explored by further investigating the non-perturbative scaling of the generated harmonics with the laser field and their bandstructure dependence since recent experimental and theoretical investigations in the literature show that high harmonic generation HHG in wide band-gap semiconductors (insulators) may lead to brighter sources due to the high laser induced carrier density and ability to withstand the driving laser fields necessary for inducing strong nonlinear and non perturbative effects leading to HHG [16–20]

II. PHOTOIONIZATION OF MONCRYSTALLINE CVD DIAMOND IRRADIATED WITH ULTRASHORT INTENSE LASER PULSE

A. Introduction

Writing graphitic electrodes inside the diamond bulk by laser irradiation is achieved in the femtosecond range, from 400 fs to 30 fs with no damage of the diamond lattice that has been reported to occur in the nanosecond range[21]. This technique is used for producing radiation tolerant three-dimensional diamond

detectors in high energy physics and small field dosimeters for radiotherapy in which a shorter interelectrode distance results in a lower voltage bias required to collect the charge produced in the diamond thickness. Because of the reduced path of the charge carriers, the charge loss is minimized and the Charge Collection Efficiency (CCE) increased, as a consequence, these detectors can be the radiation hardest sensors ever implemented [22]. Only one theoretical model on diamond graphitization has been proposed so far, involving single photon excitation above bandgap[23, 24], which is an experimental condition distant from the cited experimental conditions and applications, because irradiation below bandgap is needed to produce electrodes inside the diamond bulk.

A deep understanding of the physics of the processes is required to predictively tune the laser parameters (energy per pulse, pulse width, repetition rate), in order to obtain the sought properties of the electrodes inside the diamond bulk such as resistivity and charge collection efficiency. These are the processes of excitation and recombination of carriers, release of energy to the lattice and modification of the chemical bond. It is also critical to take into account the different crystalline qualities of the diamond samples available, which can be determined by their original optical and electronic properties.

We used a quantum theoretical model to simulate multi-photon excitation across the diamond bandgap. At the highest energies the change in optical parameters of the diamond caused by the high concentration of carriers was taken into account. Non-linear absorption causes a relevant amount of energy to be deposited prior to the focus as observed in other materials [25]. As a consequence the energy density required to the phase transition in the pure diamond bulk cannot be reached. We have shown that the theoretical model supplemented with high energy correction is in agreement with the experimental data over a very wide energy and corresponding carrier density range, resulting in the first quantitative validation of a theoretical model of multi-photon excitation of diamond to our knowledge. This result opens the way to a full understanding of laser graphitization by femtosecond pulses, a subject relevant also beyond the suggested applications. Diamond is a cardinal material with ever growing experimental applications and the process of laser graphitization is generally important, even when it is an unwanted side effect.

B. Methods, Assumptions and Procedures

For the relatively short duration of the laser pulse (30fs) considered in this work we assume the nuclei remain fixed at the lattice points during the irradiation, such that energy is absorbed from the laser field via creation of electron-hole pairs. We also neglect the contribution of impact ionization to the population of the conduction band. It has been predicted that avalanche generation in dielectrics is less important than strong-field ionization for pulse durations below 100 fs[26, 27]. However, there is experimental evidence

that optical breakdown in fused silica is dominated by avalanche ionization down to the 10 fs regime[28]. In particular the observed multiphoton ionization rates were found substantially lower than those predicted by Keldysh theory, thus identifying non-perturbative mechanism of carrier generation in bulk silica. Moreover, in a recent work on non linear absorption of femtosecond laser pulses in silica [29] transmission curves at different pulse durations have been fitted to a model taking into account multiphoton absorption and impact ionization through a modified rate equation. The results were consistent with a photon-assisted avalanche ionization rate that increases with decreasing pulse length down to a 10 fs time scale. Nevertheless the physical conditions under which the prominence of impact ionization occurs in silica will be shown to be very different from those encountered in diamond at the same laser intensities. In fact, even if the kinetic energy distribution of the photoexcited carriers extends above the required threshold, the process of impact ionization is strongly suppressed by the high population of the conduction band low energy states due to Pauli blocking and neglecting the impact ionization in our model still provides good quantitative agreement with the measured photoionization yield in diamond.

More recently, it was experimentally found that high-harmonic generation in bulk solids [30] is characteristic of a non-perturbative quantum interference process that involves electrons from multiple valence bands. Thus in order to clearly distinguish field-assisted collisional effects from coherent process in the laser-irradiated diamond, we investigate the quantum dynamics of the microscopic polarization and charge carrier distribution in one-particle framework by incorporating realistic substrate band-structure.

In long wavelength approximation we represent the light pulse by a spatially uniform time-dependent electric field. The coupling of electrons to the laser field is modeled in single-particle approximation based on the Hamiltonian

$$H(t) = \frac{1}{2}(\mathbf{p} + \mathbf{A}(t))^2 + V(\mathbf{r}) \quad (1)$$

including the periodic ion-lattice potential

$$V(\mathbf{r}) = \sum_{\mathbf{G}} V(G) \cos(\mathbf{G} \cdot \boldsymbol{\tau}) e^{i\mathbf{G} \cdot \mathbf{r}}, \quad (2)$$

where $2\boldsymbol{\tau} = a_0(1/4, 1/4, 1/4)$ is a relative vector connecting two carbon atoms in a crystal unit cell, $a_0 = 3.57\text{\AA}$ is the bulk lattice constant for diamond and \mathbf{G} labels the reciprocal lattice wave-vectors. We apply the empirical pseudopotential method to describe the atomic form factors $V(G)$ [31, 32]. Velocity gauge implied by Eq.(1) is used throughout our calculation [33] and the time-dependent electronic wavefunction is expanded over Bloch states of definite crystal momentum \mathbf{k}

$$\psi(\mathbf{r}, t) = \sum_{n\mathbf{k}} a_{n\mathbf{k}}(t) e^{i\mathbf{k} \cdot \mathbf{r}} u_{n\mathbf{k}}(\mathbf{r}), \quad (3)$$

where $u_{n\mathbf{k}}$ is the lattice-periodic part of the Bloch wave-function

$$u_{n\mathbf{k}}(\mathbf{r}) = \sum_{\mathbf{G}} e^{i\mathbf{G}\cdot\mathbf{r}} c_{n,\mathbf{G}+\mathbf{k}}, \quad (4)$$

expressed in terms of Fourier coefficients satisfying

$$\frac{1}{2}(\mathbf{G} + \mathbf{k})^2 c_{n,\mathbf{G}+\mathbf{k}} + \sum_{\mathbf{G}'} V_{\mathbf{G}-\mathbf{G}'} c_{n,\mathbf{G}'+\mathbf{k}} = \varepsilon_{n\mathbf{k}} c_{n,\mathbf{G}+\mathbf{k}}, \quad (5)$$

with eigen-energies $\varepsilon_{n\mathbf{k}}$ specifying the static substrate band structure. The time-evolution of the Fourier amplitudes

$$i\partial_t a_{n\mathbf{k}}^{(m\mathbf{k})}(t) = \varepsilon_{n\mathbf{k}} a_{n\mathbf{k}}^{(m\mathbf{k})}(t) + \sum_{n'} \mathbf{A}(t) \cdot \mathbf{p}_{nn'}(\mathbf{k}) a_{n'\mathbf{k}}^{(m\mathbf{k})}(t), \quad (6)$$

is subject to initial conditions specified long before the start of the pulse $a_{n\mathbf{k}}^{(m\mathbf{k})}(t \rightarrow -\infty) = \delta_{nm}$ and the matrix representation of the momentum operator is

$$\mathbf{p}_{nn'}(\mathbf{k}) = \mathbf{k}\delta_{nn'} - i\frac{1}{\Omega_{u.c.}} \int_{\Omega_{u.c.}} d^3\mathbf{r} u_{n\mathbf{k}}^*(\mathbf{r}) \nabla_{\mathbf{r}} u_{n'\mathbf{k}}(\mathbf{r}), \quad (7)$$

with off-diagonal matrix elements describing interband transitions, $\Omega_{u.c.} = a_0^3/4$ is the volume of the unit cell. The occupation numbers of single-particle states at time t are

$$f_{n\mathbf{k}}(t) = \sum_{m=1}^M |a_{n\mathbf{k}}^{(m\mathbf{k})}(t)|^2, \quad (8)$$

where M is the total number of initially occupied valence bands. The total number of electrons that have been photo-excited into the conduction band is given by the Brillouin zone (BZ) integral

$$n_e(t) = \sum_{n=M+1}^{\infty} \int_{\text{BZ}} \frac{d^3\mathbf{k}}{(2\pi)^3} f_{n\mathbf{k}}(t). \quad (9)$$

Charge neutrality implies that the total number of valence band holes is equal the total number of conduction electrons, i.e. $n_h = n_e$.

C. Results and Discussion

We evaluate the substrate band structure in a plane-wave basis with kinetic-energy cut-off 35 Ry. The pseudopotential form factors $V(G)$ used for diamond (in Rydbergs) are $V(G^2 = 3) = -0.625$, $V(G^2 = 8) = 0.051$ and $V(G^2 = 11) = 0.206$, here the wave-number G is given in units of $2\pi/a_0$. The time-dependent electron density is represented in a basis of static Bloch orbitals including 4 valence and 16 conduction bands, and the time-integration of the Schrödinger equation is performed by applying the Crank-Nicolson method for small equidistant time steps $\delta t \approx 1$ attosecond. The BZ integration is carried out by

a simple Monte Carlo method using 1500 randomly generated \mathbf{k} -points in a cube of edge length $(4\pi/a_0)$. The time-profile of the laser field is modeled by a Gaussian function

$$\mathbf{A}(t) = \mathbf{e}A_0 \sin(\omega_L t) e^{-\ln(4)t^2/\tau_L^2}, \quad (10)$$

where \mathbf{e} is a unit vector pointing in the direction of the electric field, the photon energy related to the driving frequency is $\hbar\omega_L = 1.55$ eV, the pulse duration is $\tau_L = 30$ fs and the field strength A_0 is given by the peak intensity of the laser field with $I = c\omega_L^2 A_0^2 / (8\pi)$ where c is the speed of light in vacuum.

In Fig.1, we show the static band structure for crystal momentum \mathbf{k} changing along the ΓX and ΓL directions in the bulk BZ. The empirical pseudopotential model reproduces quantitatively the principal energy gaps of this band structure. The location of the conduction band minimum at $\mathbf{k} \approx (0.8, 0, 0)2\pi/a_0$ corresponds to an indirect gap of 5.42 eV, that is in very good quantitative agreement with the experimental result ($E_{\text{gap}} = 5.45$ eV). Since in long-wavelength approximation the laser cannot induce a momentum changing transition, the minimal energy required to surpass the energy gap at the Γ point is 7 eV. For relatively low intensity of the laser field $I \ll 100$ TW/cm², excitation of valence electrons across this gap should occur via 5 photon absorption according to the Keldysh theory[34].

In Fig.2 we plot the time evolution of the electron density $n_e(t)$ for linearly polarized laser field directed parallel to the bonds between carbon atoms and for three different intensities $I = 1.5$ TW/cm², $I = 10$ TW/cm² and $I = 50$ TW/cm². The total number of electrons excited to the conduction band increases on the rising part of the pulse. At a later time, the charge density oscillations follow the time periodicity of the incident radiation. These transient charge oscillations are exclusively due to the time-dependent shift of the momenta of valence electrons $\mathbf{k} \rightarrow \mathbf{k} + \mathbf{A}(t)$, which adjust instantaneously (adiabatically) to the slow variation of the vector potential. Due to this velocity boost, the overlap among shifted valence and undistorted conduction bands $\langle c\mathbf{k} | v\mathbf{k}(t) \rangle$ oscillates with the periodicity of the laser field. During one half-cycle of the pulse, some fraction of electrons is transferred back into the valence band, and deviation from the adiabatic time-evolution occurs at the extrema of the electric field. The photo-ionization yield stabilizes in the wake of the pulse. Photoionization is less likely for lower field intensities ($I < 10$ TW/cm²), since valence electrons do not gain sufficient energy from the field to be excited into the conduction band. That is because of the wide bandgaps of diamond, which favor adiabatic time evolution resulting in relatively small final electron yields $n_e \sim 10^{18}$ cm⁻³. Non-adiabatic effects of electron-hole pair creation depend very sensitively on the laser intensity. When the intensity is raised above $I \geq 50$ TW/cm² the occupation of the conduction band becomes prominent resulting in high photoionization yields with $n_e \sim 10^{21}$ cm⁻³ after the conclusion of the pulse.

In Fig.3 we plot the time-dependent macroscopic polarization density $P(t) = \int_{-\infty}^t dt' J(t')$, which gives

the charge transferred into the conduction band per unit area at time t . The macroscopic current density $J(t)$ in the direction of the electric field is given by an average over the volume of the unit cell

$$J(t) = \frac{1}{\Omega_{u.c.}} \int_{\Omega_{u.c.}} d^3\mathbf{r} \mathbf{j}(\mathbf{r}, t) \cdot \mathbf{e}, \quad (11)$$

where the space- and time-dependent electron current density

$$\mathbf{j}(\mathbf{r}, t) = \sum_{m\mathbf{k}} \frac{1}{2} [\psi_{m\mathbf{k}}^*(\mathbf{r}, t)(-i\nabla_{\mathbf{r}} + \mathbf{A}(t))\psi_{m\mathbf{k}}(\mathbf{r}, t) + c.c.], \quad (12)$$

is given by the sum over initially occupied valence band orbitals. For relatively low intensity of the laser pulse $I \approx 2 \text{ TW/cm}^2$, the polarization follows adiabatically the applied electric field. For the increased pulse intensity $I = 10 \text{ TW/cm}^2$, the dielectric response of the crystal remains predominantly linear with no noticeable sustained current of delocalized electrons after the end of the pulse. When the intensity is increased to $I = 50 \text{ TW/cm}^2$, the polarization density exhibits almost linear time dependence in the wake of the pulse, showing that a DC current is generated. The induced DC current will eventually heat up the diamond lattice due to electron-phonon interactions [35] on a longer time scale, which we neglected in the present simulation.

The density of conduction band states at the end of the pulse is shown in Fig.4(a-c) for parallel polarization of the laser. For $I \sim 1 \text{ TW/cm}^2$ shown in Fig.4(a), the distribution displays isolated Lorentzian peak located at 1.5 eV above the conduction band minimum, reflecting the fact that in this regime transitions occur near the BZ centre. For the increased field intensity in Fig.4(b) $I = 10 \text{ TW/cm}^2$, the position of the low-energy peak is unaffected, however the Lorentzian profile is distorted by the laser pulse and is supplemented by additional satellite structures on the low and high energy sides of the central peak. For the higher pulse intensity $I = 50 \text{ TW/cm}^2$ shown in Fig.4(c), the density of conduction band states extends due to release of electrons with higher kinetic energies. Since the excess kinetic energy of the photoexcited carriers is above threshold for impact ionization, the subsequent energy loss during binary encounters would limit this energy distribution within the bulk. However, since large fraction of electrons have already been photoexcited close to the conduction band minimum, the scattering probability into these low-energy states is reduced due to Pauli blocking. Thus for high level of electronic excitation the probability for impact ionization should become unlikely, such that electrons can gain sufficiently high energies from the laser field.

In Fig.5 we show the photoionization yield as a function of the pulse intensity I for parallel polarization of the electric field. In the low intensity regime $I < 1 \text{ TW/cm}^2$, the electron yield increases linearly with the increase of I due to highly suppressed one-photon ionization (with negligible final densities $n_e \leq 10^{14} \text{ cm}^{-3}$). The photoionization probability increases steeply with the increase of the intensity in the range $I = 1 \text{ TW/cm}^2$ to $I = 2 \text{ TW/cm}^2$.

The slope of the theoretical curve can be fitted to $n \sim I^N$ scaling law over that range, with $N = 9$ corresponding to 9-photon ionization, showing the deviation from the perturbative scaling law I^5 occurs, pointing out that electron promotion across the diamond bandgaps is sensitive to the detailed characteristics of the substrate band-structure (cf. also [37, 38]). For $I \approx 3 \text{ TW/cm}^2$ ionization becomes unlikely, as the electron yield decreases by one-order of magnitude. That is because interband transitions occur away from the Γ point, where the wide bandgaps of diamond ($\sim 10 \text{ eV}$) suppress ionization. For increased light pulse intensities $I > 5 \text{ TW/cm}^2$, the slope of the curve flattens out as function of I . In this high-intensity regime, the momentum distribution of ionized electrons becomes more diffuse and extends over the entire Brillouin zone. When $I = 50 \text{ TW/cm}^2$ the carrier densities are $n_e \geq 10^{20} \text{ cm}^{-3}$ showing that dielectric breakdown occurs [39]. Indeed for such high conduction electron density, the corresponding bulk plasma frequency $\omega_p = (4\pi n_e)^{1/2}$ matches the laser frequency ω_L , such that electrons can absorb very efficiently energy from the light pulse via excitation of bulk plasmon resonance.

The non-perturbative I^9 scaling law in the low-intensity regime $I \sim 1 \text{ TW/cm}^2$, can be explained by we considering a simplified two-band model taking into account the three-fold degeneracy of the valence band at the Γ point, i.e.

$$\begin{aligned} i\partial_t a_{v_i} &= \mathbf{A}(t) \cdot \mathbf{p}_{v_i c} a_c(t) \\ i\partial_t a_c &= \Delta a_c + \sum_{i=1}^3 \mathbf{A}(t) \cdot \mathbf{p}_{c v_i} a_{v_i}(t) \end{aligned}$$

and $\Delta = 7 \text{ eV}$ is the bandgap. Direct interactions among valence bands vanish because of the even symmetry of their wave-functions under spatial inversion. The equation of motion for the photoionization amplitude can be integrated formally with the result

$$a_c(t) = -i \sum_{i=1}^3 \int_{-\infty}^t dt' e^{-i\Delta(t-t')} \mathbf{A}(t') \cdot \mathbf{p}_{c v_i} a_{v_i}(t') \quad (13)$$

such that the time-evolution of the valence band amplitudes becomes

$$\partial_t a_{v_i} = -\mathbf{A}(t) \cdot \mathbf{p}_{v_i c} \sum_{j=1}^3 \int_{-\infty}^t dt' e^{-i\Delta(t-t')} \mathbf{p}_{c v_j} \cdot \mathbf{A}(t') a_{v_j}(t'), \quad (14)$$

showing that the Stark mixing has introduced indirect dipole-dipole couplings among valence bands for $v_i \neq v_j$. In Fig. 6(a) we plot the time-evolution of the absolute value of the Fourier amplitudes (for laser intensity $I = 1.5 \text{ TW/cm}^2$) by neglecting the effect of induced dipole couplings. For this low intensity of the laser field, the valence band is only weakly distorted hence photoexcitation into the conduction is highly unlikely. In contrast, the strong indirect interaction among Stark-mixed valence bands enables the photoionization of bulk diamond as shown in Fig. 6(b).

The enhancement of the photoionization yield is also exhibited in the time-evolution of the optically induced interband polarization in the wake of the pulse in Fig. 6(c). Due to the induced dipole-dipole interactions between valence bands, the polarization displays rapid time oscillations with period corresponding to the bandgap energy 7 eV, otherwise it follows adiabatically the laser electric field. Thus by neglecting the induced dipole couplings, the Fourier transform of the interband polarization in Fig. 6(d) exhibits characteristic perturbative behavior, it includes 1,3 and 5th harmonics with rapidly decreasing intensities. This is in accord with the conventional Keldysh theory, which neglects energy-level degeneracies in the substrate band structure. Noticeably however, laser-induced interactions among valence bands produces non-perturbative harmonics in the Fourier transform of the induced polarization with enhanced 5th harmonic relative to the 3rd one. This effect is substantial, since the 5th harmonic is enhanced by nearly 2 orders of magnitude relative to the conventional perturbative multiphoton result. Thus dipole couplings between degenerate valence bands create a highly polarizable intermediate state that ionizes very efficiently under the light pulse to produce the free electrons in the conduction band. It is worth to note that similar results are found in Ref. [40], showing that a strong, few-cycle optical field is capable of transforming silica into a state of highly increased polarizability.

We have compared the theoretical calculations of the ionization yields n_e reported in Fig. 5 as a function of intensity I and the measured generated charge Q as a function of the energy per pulse E taking into consideration the space-dependence of the laser intensity in proximity of the beam waist. Since the charge diffusion length during the pulse is much smaller than both of the waist diameter and of the wavepacket length, we can consider the generated charge density as only dependent on the local energy density, defined as $\phi(r, z) = I(r, z)\tau_L$, with r the distance from the beam axis and z the position along the beam:

$$Q = \int_{-\infty}^{\infty} dz \int_0^{\infty} 2\pi r dr \cdot n_e(\phi(r, z)) \quad (15)$$

For a gaussian beam profile attenuated by a factor exponentially decreasing with the absorption length:

$$\begin{aligned} \phi(r, z) = & \frac{2E}{\pi w_0^2 \left(1 + \frac{z^2}{z_R^2}\right)} \exp\left[-\frac{2r^2}{w_0^2 \left(1 + \frac{z^2}{z_R^2}\right)}\right] \times \\ & \times \exp\left[-\frac{4\pi}{\lambda_0} \int_{-\infty}^z \kappa(r', z') dz'\right] \end{aligned} \quad (16)$$

where λ_0 is the wavelength in vacuum. The constant w_0 and z_R , have been evaluated measuring the size of the graphitized region of a polycrystalline diamond at the bulk graphitization threshold, which are respectively about 2-3 and 35 μm . The extinction coefficient κ has been assumed to depend on the plasma density

n_e , along with the refractive index n , according to the formulas:

$$\begin{aligned} n^2 + \kappa^2 &= n_0^2 - (\omega_p/\omega_L)^2 \\ 2n\kappa &= \omega_p^2/\omega_L^2 \frac{e}{\mu m^*} g, \end{aligned} \quad (17)$$

where $\omega_{p,L}$ are respectively the plasma and the laser frequencies, μ and m^* are the mobility and the effective mass of the charge carriers, respectively, and $g \sim 1$ is a constant, depending on the scattering mechanism [41]. In Eq. 17 a great importance is assumed by the mobility factor μ decreasing by two orders of magnitude [42] when n_e increases from 10^{16} to 10^{19} cm^{-3} . As a consequence, when the generated charge density reaches the order of 10^{19} cm^{-3} , the absorption length becomes smaller (possibly much smaller) than z_R , and the laser pulse is absorbed long before reaching the region of the laser waist. At these densities, the plasma frequency is as low as between 1/7 to 1/3 of ω_L , and the refractive index differs negligibly from its static value 2.42. This justifies the assumption of negligible reflection-diffraction effects implied by Eq. 16. Note that n_e depends on ϕ in Eq. 15, and ϕ depends on the density n_e via the extinction coefficient in Eq. 16. Self-consistency is ensured if, along each ray path, we calculate values of $\phi(r, z)$ for increasing values of z , taking into account the previously calculated values of $\kappa(r', z')$ (and thus n_e , and ϕ) for $z' < z$.

Fig. 7 shows the final comparison of theory with experimental data. The three curves reported correspond to the charge calculated from Eq. 15 with $w_0=2, 2.5$ and 3 μm , $z_R=35$ μm . The $Q(0)$ values derived from experiment, are also shown together with the theoretical charge values calculated assuming a carrier density equal to the ionization yield n_e in Fig. 5, uniformly distributed in an ellipsoidal volume element of axis $w_0 = 2.5$ μm and $z_R = 35$ μm .

D. Conclusion

We investigated theoretically the photo-ionization of monocrystalline CVD diamond subject to intense femtosecond laser irradiation and compared the simulations with experimental measurements that were carried out under the very same conditions used for preparing three-dimensional devices by fabricating conductive columnar electrodes via laser bulk graphitization. The theoretical model can explain the experimental data starting from low pulse energies and reaching about $E=0.2$ μJ , with a focus area of about 10 μm^2 . For higher intensities, up to $E=5$ μJ , the theory correctly explains the experiment when pulse absorption due to the high plasma density is phenomenologically taken into account. The agreement of the data with the theory extends over six orders of magnitude in terms of generated charge and three orders of magnitude in terms of laser intensity. The graphitization threshold is not reached in the bulk because non-linear absorption limits the intensity of the laser field and energy is deposited before reaching (i.e. upstream of)

the focus. On the contrary, when we prepare the devices the laser is initially not focused inside the diamond bulk but the conductive column is started from a localized region in the diamond surface where surface defects act as seeds. In order to fully explain the graphitization process it is mandatory to include a model for the defects involved. Our theoretical approach neglects electron-electron collisions on a femtosecond timescale which eventually cause the electron avalanching in diamond. Although all these complex mechanisms are not fully included in the simulations, we find that the experimental data is quantitatively described within our model incorporating realistic bulk band structure of diamond. Moreover we find that the Stark effect creates a highly polarizable transient state of bulk diamond that ionizes very efficiently under the light pulse. A complete understanding of the physics involved is required to tune the experimental parameters for preparing devices that can be used for particle detection and dosimetry.

III. ULTRAFAST PHOTOIONIZATION AND EXCITATION OF SURFACE-PLASMON-POLARITONS ON DIAMOND SURFACES

A. Introduction

Experimental ultrafast SPP photoexcitation on diamond surfaces was not achieved yet, even though their potential imprinting in surface relief in the form of polarization-dependent laser-induced periodical surface structures (LIPSS, surface ripples) was numerously evidenced [43–45]. Such experimental studies were devoted to the design and fabrication of bio-sensors, employing the biocompatibility of the material, by ablative surface nanostructuring of its surface with high-intensity femtosecond (fs) laser pulses, assuring precise delivery of energy, while precluding collateral thermal effects.

Generally, spatial LIPSS periods Λ are known to depend on the laser wavelength λ and the polarization of the laser electric field \mathbf{e} and the number of laser pulses [46–50, 52–54]. The surface ripple period can be slightly less than λ , resulting from the in-plane weak interference of the incident transverse fs-laser wave and nearly transverse surface polaritons [55]. These surface electromagnetic modes are photoexcited by the fs-laser pump pulse via its scattering on permanent or laser-induced (e.g., phase transition from diamond to glassy or diamond-like carbon phase) cumulative surface relief roughness [50, 52–54], or prompt laser-induced "optical roughness" [56], if the condition $\Re[\varepsilon_m] \ll -\Re[\varepsilon_d]$ is fulfilled [49, 57] for the dielectric permittivities of the photoexcited surface and the unperturbed one. Meanwhile, in the corresponding spectrally-narrow surface plasmon resonance, occurring for the photoexcited surface at $\Re[\varepsilon_m] = -\Re[\varepsilon_d]$, the short-wavelength, longitudinal surface plasmons can similarly interfere with the incident wave or among themselves (for counter-propagating quasi-monochromatic surface plasmons), inducing surface ripples with periods much lower than λ ($\lambda/2$, $\lambda/6$, ..) [49, 58–60].

Since the prompt dielectric permittivity of the photoexcited surface appears to be crucial for excitation of either near-wavelength surface polaritons, or sub-wavelength surface plasmons, prompt photoionization of diamond, directly affecting its dielectric permittivity, should be explored in details. There are numerous semi-empirical approaches to explain LIPSS formation e.g. [47, 61–64], corroborating the experimental evidence, but no genuine microscopic approach is invoked so far. The basic physical processes involve excitation of electron-hole pairs, often parameterized by Keldysh approximate formulas. Photoionization may produce highly energetic electrons that collisionally ionize the valence band and produce more electrons in the conduction band. The multiplication of carriers may cause optical breakdown of bulk diamond. The collective response of charge carriers screens out the laser electric field inside the bulk when the number density is sufficiently large. At some instant of time the bulk dielectric function may become negative at the laser wavelength, allowing excitation of SPP at the rough surface and LIPSS formation via the optical interference mechanism. The dielectric properties of the laser-irradiated material in most cases are parameterized with Drude model [52, 59, 65–68], which combines the ground state response with the laser-induced free-carrier response. This model usually requires three free parameters – the number density of electron-hole pairs, the free-carrier effective mass and the Drude damping time, which are adjusted to fit experimental data. Ref. [69, 70] proposed more elaborate model for the optical dielectric function, which implements state- and band-filling effects, renormalization of the band structure and free-carrier response. The dielectric function of laser-excited silicon was studied from first principles using the time-dependent density functional theory (TDDFT) [71]. A distinguishing feature in the linear response of the photoexcited silicon is a plasmon peak with large Drude damping time as short as $\tau_e \sim 1$ fs, despite the fact that collisional effects are neglected in the TDDFT simulation. The real part of dielectric function was well fitted by a Drude free-carrier response showing that $\Re[\epsilon_m]$ is sensitive to the total number density of excited electrons and not to the detailed distribution of electron-hole pairs, while sensitivity to the nonequilibrium distribution of the phototexcited carriers manifests in the imaginary part of the dielectric constant. Subsequently, TDDFT was applied to study ablation of silica subjected to ultrashort laser pulses [72]. The comparison between the estimated surface ablation threshold and the experimental data suggests a non-thermal mechanism in the laser ablation of silica by fs-laser pulses, furthermore theoretical ablative crater depths agree with the measured ones. The drawback of this approach is its limitation to very short laser-matter interaction timescales (less than 10 fs).

We present theoretical results for the laser ablation and subsequent LIPSS formation on diamond surfaces subjected to normally incident 515-nm, 200-fs laser pulses due to the excitation of SPPs. Our theoretical modeling of LIPSS formation on diamond surfaces is based on numerical solution of the time-dependent Schrödinger equation (TDSE) in bulk diamond subjected to a single intense laser pulse. The theory describes the electron dynamics quantum mechanically in the single-active-electron approximation.

Collisional de-excitation of the photoexcited carriers and subsequent impact ionization are treated within rate equation approach and an optical breakdown threshold is derived. Due to the contribution of the impact ionization the real part of the bulk dielectric constant of the irradiated diamond becomes negative in the trailing edge of the pulse resulting in plasma that is opaque to the incident radiation. The inhomogeneous energy deposition in the surface was modeled with the Sipe-Drude efficacy factor theory [64, 67] in terms of time-dependent dielectric function of free carriers. The applicability of this efficacy factor theory for LIPSS formation in laser-irradiated dielectrics was confirmed by numerical solutions of the Maxwell's equations at statistically rough surfaces [73].

B. Methods, Assumptions and Procedures

In order to model theoretically LIPSS formation in femtosecond-laser-excited diamond, we apply the *ab initio* theory developed by Sipe [47]. In this picture, the laser beam is incident on a rough surface, the (permanent or laser-induced) roughness is assumed to be confined within a surface region (selvedge) of thickness l much smaller than the laser wavelength λ . The optically-induced polarization in the selvedge generates surface-scattered waves that interfere with the refracted laser beam leading to inhomogeneous energy deposition into the surface. The inhomogeneous energy absorption can be described by the function

$$A(\boldsymbol{\kappa}) \sim |b(\boldsymbol{\kappa})|\eta(\boldsymbol{\kappa}; \boldsymbol{\kappa}_i), \quad (18)$$

where $\boldsymbol{\kappa}_i$ is the component of the laser propagation wave vector parallel to the surface, $b(\boldsymbol{\kappa})$ is a measure of surface roughness at wave-vector $\boldsymbol{\kappa} = (\kappa_x, \kappa_y)$ and $\eta(\boldsymbol{\kappa}; \boldsymbol{\kappa}_i)$ is an efficacy factor describing the contribution to the energy absorption at the LIPSS wave vector $\boldsymbol{\kappa}$. The prediction of Eq.18 is valid if the selvedge thickness is small compared to the LIPSS period, i.e. $\kappa l \ll 1$ should be satisfied. The efficacy factor essentially incorporates the modification of the surface morphology and the variation of the dielectric constant ε of the photoexcited diamond. For normally incident s-polarized laser pulse with $\boldsymbol{\kappa}_i = \mathbf{0}$, the efficacy factor (as a function of the normalized wave-number $\kappa = \lambda/\Lambda$) can be written as $\eta(\boldsymbol{\kappa}) = 4\pi|\Re e[\nu(\boldsymbol{\kappa})]|$ with

$$\nu(\boldsymbol{\kappa}) = \left[h_{ss}(\kappa) \left(\frac{\kappa_y}{\kappa} \right)^2 + h_{\kappa\kappa}(\kappa) \left(\frac{\kappa_x}{\kappa} \right)^2 \right] \gamma_t |t_s|^2, \quad (19)$$

where the response functions h_{ss} and $h_{\kappa\kappa}$

$$h_{ss}(\kappa) = 2i \frac{\kappa\kappa_m}{\kappa_v + \kappa_m}, \quad h_{\kappa\kappa}(\kappa) = 2 \frac{\kappa_v\kappa_m}{\varepsilon\kappa_v + \kappa_m}, \quad (20)$$

are given in terms of the transient bulk dielectric function $\varepsilon(\omega; t)$, $\kappa_v = \sqrt{\kappa^2 - 1}$ and $\kappa_m = \sqrt{\kappa^2 - \varepsilon}$, the Fresnel transmission coefficient $t_s = 2/(1 + \sqrt{\varepsilon - 1})$ in the absence of the selvedge, the effective transverse susceptibility function $\gamma_t = (\varepsilon - 1)/4\pi \{ \varepsilon - (1 - f)(\varepsilon - 1)[h(s) - Rh_I(s)] \}$, the surface

roughness characterized by shape s and filling f factors, $R = (\varepsilon - 1)/(\varepsilon + 1)$ and the shape functions $h(s) = \sqrt{s^2 + 1} - s$, $h_I(s) = (\sqrt{s^2 + 4} + s)/2 - \sqrt{s^2 + 1}$. When $\Re[\varepsilon] < 0$, the response function h_{ss} exhibits small kinks near the light line $\kappa \approx 1$, in contrast $h_{\kappa\kappa}$ exhibits sharp resonance structure due to the excitation of surface plasmons and diverges at the (complex) SPP wave-number $\kappa_{SPP} = \omega/c\sqrt{\varepsilon/(1 + \varepsilon)}$.

As in section II photoexcitation and the dielectric response of laser-irradiated diamond are treated in independent particle approximation based on the 3D TDSE. In a long-wavelength approximation the light pulse is represented by a spatially uniform time-dependent electric field and velocity gauge is used throughout the calculations [74]. The static bulk band structure is represented by the lowest 4 valence bands and 16 unoccupied conduction bands. The Brillouin zone was sampled by a Monte Carlo method using 2000 randomly generated \mathbf{k} -points. The time step for integration of the equations of motion was $\delta t = 0.03$ a.u.

For the static band structure shown in Fig.1 carrier excitation occurs through the direct gap at the Γ point, however excitation into higher lying conduction bands is also a relevant process for the considered laser intensity range $I \in [1, 50]$ TW/cm².

During the irradiation of the diamond surface with pulsed 200 fs-laser, the total number of electrons generated into the conduction band is given by a Brillouin zone integral

$$\rho_e(t) = \sum_{\epsilon_n > 0} \int_{\text{BZ}} \frac{d^3\mathbf{k}}{4\pi^3} f_{n\mathbf{k}}(t), \quad (21)$$

where $f_{n\mathbf{k}}$ is the occupation number of the n -th conduction band and \mathbf{k} is the crystal momentum. The electronic excitation energy per unit cell is given by

$$E_{ex}(t) = \sum_{\epsilon_n < 0} \int_{\text{BZ}} \frac{d^3\mathbf{k}}{4\pi^3} \langle \psi_{n\mathbf{k}}(t) | i\partial_t | \psi_{n\mathbf{k}}(t) \rangle - E_0, \quad (22)$$

where $\psi_{n\mathbf{k}}(t)$ are the time-evolved Bloch orbitals of valence electrons and E_0 is the ground-state energy. The time evolution of the free-electron density is shown in Fig. 8a, for linearly polarized electric field along the (1,1,1) direction with intensity 30 TW/cm². Carrier generation occurs efficiently prior to the peak of the pulse. Transient charge density oscillations following the laser period are due to quiver motion of free electrons in the electric field. An electron-hole plasma (EHP) with number density exceeding 10^{21} cm⁻³ is established shortly after the peak intensity. The cycle-averaged photoelectron yield, shown in Fig. 8b, is a slowly varying function of time. Carrier generation on the rising edge of the pulse competes with recombination on the trailing edge of the pulse to determine the final photoionization yield. Recombination of carriers becomes unlikely with the increased laser intensity, cf. also Fig. 8b. The cycle averaged electron yield includes contributions due to creation of real as well as virtual electron-hole pairs. Since adiabatic evolution does not produce any real excitation of the crystal, the carrier density should be calculated with respect to adiabatically evolved ground state orbitals that are obtained from the static Bloch orbitals with

shifted crystal momentum $\mathbf{k}(t) = \mathbf{k} + \mathbf{A}(t)$, i.e. $\rho(t) = \rho_e(t) - \rho_{ad}(t)$, where the adiabatic density is

$$\rho_{ad}(t) = \sum_{\epsilon_n < 0} \int_{\text{BZ}} \frac{d^3\mathbf{k}}{4\pi^3} |\langle u_{n\mathbf{k}} | u_{n\mathbf{k}(t)} \rangle|^2, \quad (23)$$

and $\{|u_{n\mathbf{k}}\rangle\}$ are the lattice-periodic Bloch states. The number density of photoexcited carriers is shown in Fig. 8c. It can be seen that discarding contributions of virtually excited electron-hole pairs leads to reduction in the number density by an order magnitude near the peak of the pulse. The electronic excitation energy is shown in Fig. 9(a) for laser intensity 30 TW/cm². The temporal variation of the cycle-averaged energy gain follows closely the envelope of the laser pulse during the first half of the driving pulse and reaches 1.5 eV/atom at the peak of the pulse that is small as compared to the cohesive energy of diamond 7.37 eV/atom. After the pulse peak, electron-hole pairs recombine by transferring part of their energy back to the radiation field. Energy exchange is not completely reversible since the time delay in restoration of equilibrium gives rise to a net energy gain of 0.5 eV per carbon atom after the end of the pulse. The deposited energy increases steadily with the increase of the intensity, i.e. for I=50 TW/cm², it reaches 2 eV/atom. Since this excitation energy is still lower than the diamond cohesive energy, Fig. 9(b) shows that ablation threshold is not reached up to I=50 TW/cm².

For the 200fs pulse duration and intensities lower than 50 TW/cm² the electron density produced by photoionization is below the critical one. That suggests that impact ionization is the relevant process that determines the optical breakdown threshold. In Fig.10 (a-c) we plot the density of conduction states after the end of the pulse. It is seen that the laser has created electron-hole pairs with well-defined energies. This non-thermal distribution relaxes towards the equilibrium Fermi-Dirac distribution on a time scale ranging over few tens of a femtoseconds to a picosecond [75, 76] without changing the electron number density. Photoelectrons are excited into the lowest conduction band across the direct gap (with energies 2 eV above the conduction band minimum) and substantial fraction of carriers occupy higher lying conduction bands with energy above threshold for impact ionization (specified by the indirect gap 5.4 eV). These highly energetic electrons may collisionally de-excite to lower energy states and their excess energy is spent to promote valence electrons into the conduction band. Assuming that the time evolution of the electron density is governed by a rate equation [77, 78]

$$\frac{d\rho}{dt} = G(t) - R(t) + w_{imp}(I)\rho \quad (24)$$

including carrier generation $G(t)$ and recombination $R(t)$ rates supplemented by an intensity-dependent impact ionization rate w_{imp} obtained as a weighted-average of the field-free ionization rate

$$w_{imp}(I) = \frac{\int_{\epsilon_i}^{\infty} d\epsilon \rho(\epsilon; I) P_{imp}(\epsilon)}{\int_0^{\infty} d\epsilon \rho(\epsilon; I)} \quad (25)$$

here $\rho(\epsilon; I)$ is the density of conduction states after the end of the pulse (cf. Fig.10a-c),

$$\rho(\epsilon; I) = \sum_{\epsilon_n > 0} \int_{\text{BZ}} \frac{d^3\mathbf{k}}{4\pi^3} f_{n\mathbf{k}}(I) \delta(\epsilon - \epsilon_{n\mathbf{k}}), \quad (26)$$

$P_{imp}(\epsilon) = P_0(\epsilon - \epsilon_i)^{4.5}$ is the energy-dependent impact ionization rate for diamond, ϵ_i is the threshold for impact ionization (5.42 eV) and $P_0 = 3.8 \times 10^{10} s^{-1} eV^{-4.5}$ [79].

In contrast to the standard perturbative result based on Keldysh theory valid for monochromatic laser radiation the calculated carrier generation and recombination rates shown in Fig.11a do not follow the temporal profile of the laser pulse. This result suggests that the pulse shape and pulse duration are relevant control parameters for non-adiabatic electron dynamics in the laser irradiated diamond. The key features are generation of dense plasma 50fs prior to the pulse peak and subsequent laser-induced recombination of electron-hole pairs in the trailing edge of the pulse.

Fig.11b shows the impact ionization rate that depends in highly non-linear way on the laser intensity. This non-linear and non-monotonic intensity-dependence reflects the population of higher-lying conduction bands (cf. also Fig.10). It is seen that the impact ionization rate reaches few tens of inverse picosecond for $I > 15 \text{ TW/cm}^2$. In Fig.12 we plot the EHP density with and without the impact ionization term. This comparison demonstrates that photoionization produces the seed electrons needed for the impact ionization on the rising edge of the pulse and then the conduction electron density grows exponentially after the pulse peak resulting in dense plasma (with density 10^{22} cm^{-3}) 50fs after the peak of the pulse.

Since the absorption of the femtosecond laser pulses in diamond results in the generation of nearly free electrons in the conduction band on timescales smaller than the electron-phonon relaxation time [80], we describe the linear response of the photoexcited diamond by a free-carrier Drude response [67] using of time-dependent plasmon-pole-approximation for the density-density correlation function of the Coulombically interacting electron gas [81]

$$S(t, t') = -\theta(t - t') \omega_p^{3/2}(t') \omega_p^{-1/2}(t) \sin \int_{t'}^t d\tau \omega_p(\tau), \quad (27)$$

where $\theta(t)$ is the Heaviside step function, $\omega_p(t) = \left(\frac{\rho(t)}{\epsilon_0 m_e} \right)^{1/2}$ is the bulk plasma frequency, ϵ_0 and m_e are the vacuum permittivity constant and the free-electron mass, respectively. In long wavelength approximation the spatial dispersion of the bulk plasmon is neglected. The Fourier transformation of the correlation function is the transient frequency dependent inverse dielectric function of the free-electron plasma

$$\varepsilon^{-1}(\omega; t) = 1 + \int_{-\infty}^t dt' e^{i(\omega + i\delta)(t-t')} S(t, t'), \quad (28)$$

where $\delta = 1/\tau_e$ is a free-carrier polarization dephasing rate, which we shall treat as a free parameter. If the time delay in the build up of screening in the optically excited plasma can be neglected, the classical Drude

dielectric function is recovered $\varepsilon^{-1}(\omega; t) = \omega^2 / (\omega^2 - \omega_p^2(t))$ with parametric time dependence of the bulk plasma frequency.

In Fig.13a-c, we plot the real and imaginary parts of the dielectric function for laser intensity 18 TW/cm². The screening charge density accumulates during the first half of the pulse ($t < 0$). Over that time interval the laser frequency is above the plasma frequency and the diamond surface remains transparent to the incident radiation. The frequency dependent dielectric function displays oscillations in the spectral range below the laser frequency due to the time lag in the build up of screening. Because of the impact ionization, the laser frequency falls off below ω_p after the pulse peak ($t = 25$ fs) when the plasma is reflective for the incident radiation and an optical breakdown threshold is reached. In this regime, the dielectric function essentially exhibits the Drude form with time-dependent bulk plasma frequency $\omega_p(t)$. For the transiently increasing carrier density, $\Re[\varepsilon]$ passes the narrow surface plasmon resonance at $\Re[\varepsilon] = -1$, with $\kappa_{SPP} \gg 1$ and $\Lambda/\lambda \ll 1$, and becomes large and negative in the trailing edge of the pulse ($t > 100$ fs) with $\Im[\varepsilon] > 0$, with corresponding $\kappa_{SPP} \geq 1$. During this plasmonically-active phase of the laser-irradiated diamond the SPP-laser interference mechanism of inhomogeneous energy deposition is effective and leaves permanent imprints on the surface morphology after the conclusion of the pulse.

C. Results and Discussion

To make possible identification and interpretation of experimentally obtained SPP modes we plot the efficacy factor as a function of the wave vector κ in a narrow laser intensity range above the optical breakdown threshold in Fig.14 a-b. The transient bulk dielectric function was evaluated at the laser wavelength, i.e. $\varepsilon(t) = \varepsilon(\omega_L; t)$. The surface roughness was modeled as a collection of spherically-shaped islands corresponding to standard values $s = 0.4$ and $f = 0.1$ for the shape and filling factors respectively. For normally incident light pulse, the numerical results are weakly dependent on the specific parameters describing surface morphology and therefore the transient dielectric constant is the most significant in determining the efficacy factor. Here we demonstrate that the main features in the inhomogeneous energy deposition in the surface as represented by the position of the peaks of the transient efficacy factor are in correspondence with the experimentally observed LIPSS periods.

In a very narrow laser intensity range, when the laser frequency nearly matches the surface plasma frequency (Fig. 14a), the efficacy factor has large contribution due to excitation of the surface plasmon resonance (SPR). In this early stage, the spatial extension of the electromagnetic field inside the bulk associated with SPP is determined by the SPR decay constant κ_m , which at short wavelengths $\kappa_m \rightarrow 1/l$ defines a skin-depth $l_s = 1/\kappa_m \sim l$ leading to strong concentration of the electromagnetic field in the thin selvage

region. SPPs need finite time to build up to incorporate the details of the surface relief and interfere with the laser to modify the Fourier components of the surface roughness function $b(\boldsymbol{\kappa})$ via periodic laser ablation. In this regime the deposition of laser energy into the surface plasmon wavevector causes formation of fine ripples with spatial periods around 100 nm, as observed in the periphery of the ablative craters, cf. Fig.16. The transverse-magnetic characteristic of the SPP determines the orientation of the surface ripples. At a later time, the transiently increasing number of conduction electrons makes the dielectric constant large and negative at the laser wavelength, the intensity map of $\eta(\boldsymbol{\kappa}; \mathbf{0})$ shrinks and concentrates on the outer part of the circle $\kappa = 1$ (cf. Fig 14b) which clearly can be associated with the formation of near-wavelength surface ripples oriented perpendicularly to the laser polarization. At the longer wavelengths with $\kappa \rightarrow 0$ the skin depth $l_s = c/\omega_p \approx 80$ nm is much smaller than the laser wavelength. Therefore, above the SPR excitation threshold, the transiently increasing carrier density results in a shift of the SPP wave number from the high spatial frequency region towards the light line (also causing expansion of the skin depth), and this red shift is highly sensitive on the carrier density (or laser intensity), cf. Fig.15a. The surface plasmon peak in the efficacy factor is also affected by the relaxation time parameter τ_e as shown in Fig. 15b from the experiments described in . If τ_e is decreased to 10 fs, the surface plasmon cusp turns into a dip, which hinders the efficient energy absorption at the surface plasmon wavevector. This dependence suggests that the Drude carrier relaxation time parameter influences prompt feedback mechanisms involved in the formation of surface ripples. Indeed in the high-frequency limit with $\omega_L \tau_e \gg 1$, the metalized surface behaves as a nearly ideal inductor, while in the low-frequency limit $\omega_L \tau_e \ll 1$, the resistive Ohmic losses result in electron heating in the skin layer.

Because the efficacy factor theory does not fully account for interpulse feedback processes that are undoubtedly important in the detailed development of morphological features on the diamond surface our theoretical results are not directly applicable to the multipulse phase of LIPSS formation. However the experimental data shows that once surface ripples are formed, exposure by subsequent pulses has little effect on their spatial period and location, thus LIPSS formation should be possible already for a single-pulse irradiation, provided that SPP can be excited, e.g., by surface defects [83]. Once LIPSS are formed, the spectrum of the surface roughness, $b(\boldsymbol{\kappa})$ contains peaks at the SPP wavenumber causing enhanced inhomogeneous energy deposition and further growth of LIPSS as is also evidenced from the SEM images in Fig.16a-b. Furthermore the subsequent pulses interact with periodically structured surface hence a grating-assisted laser-surface coupling becomes effective [49] causing a decrease of the ripple wavelength. The experimental data shows only minor modification of LIPSS periods that is consistent with the hypothesis in Ref. [49] that because of strong thermal effect at the crater center, the grating-assisted coupling is weak and the ripple wavelength is unaffected by higher exposure, i.e. depends weakly on the superimposed pulse

number.

D. Conclusion

In this section the transition of diamond into plasmonically-active material and the subsequent formation of ripples on its surface caused by SPP-laser interference were investigated via first principle approaches. The numerical simulations of periodic laser energy deposition on photo-excited diamond surface revealed the formation of fine ripples oriented perpendicularly to the laser polarization in a narrow range of intensities above the optical breakdown threshold. The transient increase of the carrier density above this threshold resulted in the formation of near-wavelength surface ripples. In addition we demonstrate that transient changes of the dielectric permittivity reflect the chronological order of the ripple formation. Semi-quantitative agreement with the experimentally observed periods of the periodic structures was obtained. The realistic insight into the microscopic processes gained by our combined theoretical and experimental study will allow to predict and potentially extend the capabilities of the dielectric nano-optical meta devices and the photo-modulated metasurfaces based on them.

IV. HIGH HARMONIC GENERATION FROM BULK DIAMOND DRIVEN BY INTENSE FEMTOSECOND LASER PULSE

A. Introduction

High harmonic generation is a secondary process of laser frequency conversion to its multiples driven by the coupling of the oscillating electric field of an intense ultrashort laser pulse to electrons comprising matter. The microscopic mechanisms underlying this phenomenon have been elucidated experimentally demonstrating that high intensity laser pulses in the UV and IR spectrum generate high order harmonics in gaseous and molecular targets [84–88], plasmas [89] and in solid materials [16]. These experiments have shown that sources based on high harmonic generation (HHG) have spatial and temporal coherence, high directionality and polarization but due to the low efficiency of the process, the intensities of the generated harmonics are orders of magnitude lower than that of the exciting field hence less intense than EUV, XUV and soft x-ray radiation produced in the huge facilities such as FEL accelerator [90] and Synchrotron Radiation (SR) [91]. Nevertheless they can be potentially used to obtain coherent radiation of sub-femtosecond to attosecond duration in a broad wavelength range (XUV to X-ray) [92–94] capable of inducing physical processes on very short time and space scales leading to applications such as attosecond electron dynamics [95], molecular tomography and protein crystallography [96], etc.

Experimental studies of HHG in semiconductors and dielectrics have been reported recently, e.g. [16–18]. In solid crystals the interplay between generation of carriers via multiphoton excitation over the bandgap at high intensities leading to catastrophic breakdown of the material and HHG is carefully explored to find regimes in which only HHG takes place avoiding material collapse. In the pioneering study of Ghimire et al. [16] long wavelength laser radiation is used to suppress multiphoton ionization and to obtain HHG. Experimental and theoretical study of HHG spectra from rare-gas solids [17] exposed characteristic features of HHG in solids: abrupt appearance of a second plateau as the driving laser intensity increases over a narrow intensity range that consists of a few harmonics; complicated dependence of the cutoff of both plateaus on the laser field, i.e. following neither linear (solid phase) nor the square-root scaling (gaseous phase); photon energy of the HHG in solids exceeding the maximum band separation between the highest-valence and lowest-conduction bands. Studies based on a model describing electrons tunneling from the valence to a single conduction band where they are accelerated by the driving laser field and experience Bragg reflections from the edge of the Brillouin zone [97, 98] Interband transitions as well as interband coherences between conduction bands and valence bands were taken into consideration in other models [99–101] In the recent theoretical approaches used to rationalize HHG in crystalline solids including HHG in diamond varying from Time Dependent Density Functional Theory (TDDFT), [19, 20, 102, 103] Time dependent Schrodinger equation (TDSE) [100], band resolved Semiconductor Bloch equations [101, 104] to semiclassical methods [105] the latter being more intuitive than the former, the underlying microscopic processes are still explored to elucidate further the dependence of HHG in solids on the electronic band structure and on the interplay between inter- and intraband transitions as well as on the collective behavior of the high density electrons and holes coupled to the lattice. In this respect methods using TDSE including full band structure treatment together with saddle point methods may provide very consistent and thorough theoretical treatment of the HHG generation from solid phase. In view of the fact that HHG in wide band-gap semiconductors may lead to brighter sources due to the high laser induced carrier density and ability to withstand the driving laser fields necessary for inducing strong nonlinear and non perturbative effects leading to HHG in the present work we explore the feasibility for femto and attosecond pulse generation from diamond subjected to intense 15 fs laser pulse with mid-infrared wavelength by exploring further and deeper the non-perturbative scaling of the generated harmonics with the laser field and their bandstructure dependence.

B. Methods, Assumptions and Procedures

In velocity-gauge, the TDSE in single-active electron approximations is given by

$$i\frac{d}{dt}|\psi_{v\mathbf{k}}(t)\rangle = (H_0 + H_{\text{int}}(t))|\psi_{v\mathbf{k}}(t)\rangle \quad (29)$$

where $v\mathbf{k}$ labels the initially occupied valence band states of definite crystal momentum \mathbf{k} , H_0 is the Hamiltonian of the undistorted lattice

$$H_0 = \frac{1}{2}\mathbf{p}^2 + V(\mathbf{r}), \quad (30)$$

and

$$H_{\text{int}}(t) = \mathbf{A}(t) \cdot \mathbf{p} \quad (31)$$

is the interaction Hamiltonian between the laser field and the electron, \mathbf{p} is the momentum operator and $V(\mathbf{r})$ is the periodic ion-lattice potential. The vector potential is parametrized by a Gaussian function as in section II. The eigenstates of the field-free Hamiltonian are Bloch states of definite crystal momentum

$$H_0|n\mathbf{k}\rangle = \varepsilon_{n\mathbf{k}}|n\mathbf{k}\rangle. \quad (32)$$

We expand the time-dependent states over this basis

$$|\psi_m(t)\rangle = \sum_{n\mathbf{k}} |n\mathbf{k}\rangle \langle n\mathbf{k}|\psi_m(t)\rangle \quad (33)$$

and calculate the optically-induced electron current in direction of the laser electric field is given by the Brillouin zone integral

$$J(t) = \int_{\text{BZ}} \frac{d^3\mathbf{k}}{4\pi^3} J(\mathbf{k}, t) \quad (34)$$

where

$$J(\mathbf{k}, t) = \sum_v \langle \psi_{v\mathbf{k}}(t) | \mathbf{e} \cdot \mathbf{p} | \psi_{v\mathbf{k}}(t) \rangle, \quad (35)$$

the diamagnetic gauge current contribution can be neglected, because it does not contribute to generation of high harmonics. The HHG spectrum can be presented as a coherent sum

$$I(\omega) = \left| \int_{\text{BZ}} \frac{d^3\mathbf{k}}{4\pi^3} J_{\mathbf{k},\omega} \right| \quad (36)$$

over contributions from recombination of electron-hole pairs with wave-vector \mathbf{k}

$$J_{\mathbf{k},\omega} = \int dt e^{i\omega t} J(\mathbf{k}, t). \quad (37)$$

The valence electron states are propagated in time for small equidistant steps of $\delta = 0.7$ attoseconds by applying the Cayley transformation

$$|\psi_v(t + \delta)\rangle \approx \left(I - i\frac{\delta}{2}H(t) \right)^{-1} \left(I + i\frac{\delta}{2}H(t) \right) |\psi_v(t)\rangle \quad (38)$$

where I is the unit matrix.

C. Results and Discussion

Fig.17(a-c) shows HHG spectra for three laser intensities $I = 2, 10$ and 30 TW/cm^2 . For the low intensity shown in Fig.17(a), the HHG is characterized by odd harmonic structure due to the inversion symmetry of the diamond lattice and consists of the 1st and 3rd sub-bandgap harmonics and the 5th harmonic. Since the direct band gap at the Γ -point is nearly 7 eV, the lowest excitation of valence electrons across this gap occurs via 5 photon absorption. At this lower intensity, the HHG ends abruptly at the position of 5th harmonic, such that the high-energy cutoff is determined by the direct gap. For the increased intensity shown in Fig.17(b), the spectrum extends to higher harmonic orders, a single plateau is seen with cut-off at the position of 9th harmonic. Noticeably individual harmonics exhibit fine structure, similarly to the results reported for the gas phase [106]. For the highest intensity 30 TW/cm^2 shown in Fig.17(c), a second plateau suddenly emerges with cutoff positioned at the 50th harmonic. The appearance of second plateau with harmonic orders extending beyond the atomic limit of the corresponding gas-phase harmonics indicates strong dependence of HHG on the band structure of diamond. Similar results are found in HHG spectra from rare-gas solids [17].

Fig.18(a-b) shows the field-dependence of the photon-energy cutoff for the first and second plateau, respectively. In contrast to the cutoff law observed for gas-phase harmonics, cutoff harmonics generated from diamond bulk display almost linear scaling with the field strength F . This linear scaling law is consistent with experimental observations in ZnO [16]. The high-energy cutoff of the second plateau is distinguishable for strong fields with $F \sim 0.4 \text{ V/\AA}$ corresponding to laser intensity $I > 10 \text{ TW/cm}^2$. The slope of this linear dependence implies that the cutoff energy increases by 2 harmonic orders when the field strength is increased by 0.5 V/nm . In contrast, the slope of the photon-energy cutoff of the first plateau is flatter by a factor of 3. Numerical results show saturation of the cutoff of the first plateau for field strength $F \geq 1 \text{ V/\AA}$.

In Fig.19 we plot the field dependence of the spectral intensity of individual harmonics S_n from the first plateau. The laser intensity dependence can be divided into 3 regimes. I. Perturbative regime: The 3rd and the 5th harmonic are distinguishable and scaling law $S_n \sim F^n$ is exhibited. II. Intermediate regime (with $F \sim 1 \text{ V/nm}$): The HHG spectrum extends to higher orders as the field strength increases. The intensity of

different harmonic orders show the same power law $S_n \sim F^6$ regardless on the harmonic order. III. High field strength with $F \geq 5$ V/nm: the intensity of individual harmonics become indistinguishable.

To gain insight into the underlying microscopic mechanisms of hhg in diamond we plot in Fig.20(a-c) presents the time evolution of the current density distribution for three different laser intensities $I = 2, 10$ and 30 TW/cm². In the perturbative regime shown in Fig.20(a), the current density follows quasi-adiabatically the laser vector potential, i.e.

$$J(t) \approx J^{\text{ad}}(t) = \sum_{v, \mathbf{k}} \mathbf{e} \cdot \nabla_{\mathbf{k}} \varepsilon_v(\mathbf{k}) \Big|_{\mathbf{k}=\mathbf{k}(t)} \quad (39)$$

where $\mathbf{k}(t) = \mathbf{k} + \mathbf{A}(t)$ is shifted crystal momentum and $\varepsilon_v(\mathbf{k})$ are the dispersion curves for valence electrons. For the intermediate regime in Fig.20(b), the time evolution of photoexcited carriers near the BZ edges remains adiabatic due to the wide band gaps of diamond, however states near the BZ center do not have enough time to fully equilibrate against the laser vector potential $A(t)$, such that the current density is strongly distorted after the peak of the pulse. This distortion expresses the non-adiabatic effects of electron-hole pair excitation. The nonlinear polarization current undergoes rapid changes on a sub-femtosecond time scale tracing out the burst of emitted high harmonics after the peak of the pulse. For high field strength with intensity $I = 30$ TW/cm², the prompt excitation of electron-hole pairs becomes highly likely as shown in Fig.20(c) and the non-adiabatic distortion of the current density extends over higher momentum states in the BZ.

The Fourier transform of the even part of the current density $I(\mathbf{k}, \omega) = |J_{\mathbf{k}\omega} + J_{-\mathbf{k},\omega}|$ along the Γ -L line is shown in Fig.21(a-c). The odd harmonic structure of HHG is due to the destructive interference of even order harmonics. For the lowest intensity in Fig.21(a), sub-bandgap harmonics extend from the BZ center towards the edges; the recombination of electron-hole pairs near the BZ center gives rise to intense emission of 5th harmonic, while the 7th order is highly suppressed. For higher laser intensity of 10 TW/cm² in Fig.21(b), it is seen that the HHG spectrum is characterized by a plateau region above the bandgap with the plateau terminating abruptly at the position of the 9th harmonic. The numerical results reveal that the plateau and the high-energy cutoff converge when the lowest number of conduction bands included in the calculation is 8. Thus we confirm that HHG depends sensitively on details of the band structure and is characterized by strong coupling involving multiple single-particle states. For the highest intensity shown in Fig.21(c), the spectrum extends to high harmonic orders. The two plateau regions can be distinguished, the first one extends to 15th order, decreases gradually in spectral intensity with the increase of the harmonic order and crosses over into the second plateau with harmonics extending above the 40th order.

To non-adiabatic electron dynamics associated to HHG in the intermediate regime corresponding to

laser intensity 10 TW/cm^2 is shown in Fig. 22(a-c). Fig. 22(a) shows the temporal profile of the nonlinear current corresponding to 5-photon transition from the light-hole into the lowest conduction band ($n_c = 1$). The current waveform follows adiabatically the laser vector potential during the first part of the pulse and is distorted 2 fs prior to the peak of the pulse; the subsequent rapid sub-cycle oscillations represent the build up of coherent superposition of populations in the light-hole and the conduction band; steady-state dipole oscillations remain after the end of the pulse. In a similar way the laser-induced hybridization of the light-hole with a higher-lying conduction band ($n_c = 2$) creates rapid dipole oscillations on an attosecond time scale, cf. Fig. 22(b). After the peak of the pulse, the enhanced steady-state non-adiabatic current gives rise to emission of intense 7th harmonic. Fig. 22(c) shows the nonlinear current corresponding to transitions into and out of the $n_c = 5$ conduction band, noticeably the peak of the current is delayed by 5 fs after the peak of the pulse, the time profile shows that the 9th cutoff harmonic is highly virtual and exists only during the second half of the pulse. Similar results are found in the strong-field regime with high harmonic orders due to transitions into and out of highly excited conduction band states. In order to gain further insight into the microscopic mechanism of the harmonic generation we separate the electron dynamics into interband and intraband processes. For that reason we expand the current Eq.35 into intraband contribution:

$$J_{intra}(t) = \sum_{n\mathbf{k}} f_{n\mathbf{k}}(t)(\mathbf{e} \cdot \mathbf{v}_{n\mathbf{k}}) \quad (40)$$

where $v_{n\mathbf{k}} = \partial\varepsilon_{n\mathbf{k}}/\partial(\mathbf{k})$ and interband contribution of the induced transient photocurrent

$$J(\mathbf{k}, t) = \sum_{nn'} \rho_{nn'}(\mathbf{k}, t)(\mathbf{e} \cdot \mathbf{p}_{nn'}(\mathbf{k}) + A(t)\delta_{nn'}) \quad (41)$$

where $\mathbf{p}_{nn'}$ is the matrix representation of the momentum operator and

$$\rho_{nn'\mathbf{k}}(t) = \sum_{m=1}^M \langle n\mathbf{k}|\psi_m(t)\rangle\langle\psi_m(t)|n'\mathbf{k}\rangle \quad (42)$$

is the density matrix of Bloch electrons.

In Fig.23 the harmonic spectrum for intraband and interband currents for three different laser intensities $I = 2, 10$ and 30 TW/cm^2 is shown. In Fig.23 (a) is seen that for the subbandgap harmonics (first and third harmonics) the contributions from intraband and interband currents nearly cancel out resulting in low total current causing the intensities of the fundamental and the third harmonics to be significantly reduced. As can be clearly seen from Fig.23 (a) (b) and (c) the higher harmonics (starting from the fifth harmonic) are due to interband transitions since the the interband current predominates over the intraband current. It

clearly seen that the spectral intensity of the intraband current decreases drastically after the 21 harmonic order (at the first plateau). At the second plateau its spectral intensity drops off a few orders of magnitude in respect to the contribution from the interband current as seen from Fig.23 (c). Therefore we conclude that the interband process is the dominant one for the harmonic generation after the 5th harmonic order. The time-profile of the polarization current generating the 5th harmonic for the three different intensities - for three different laser intensities $I = 2, 10$ and 30 TW/cm^2 is shown in Fig. 24. Clearly harmonic generation occurs after the peak of the driving pulse, the pulse duration of that harmonic is shorter than the fundamental period τ_L . The fine structure of individual harmonics is imprinted in the transient modulation of the non-linear electronic current on a femtosecond timescale.

D. Conclusion

We presented calculation of HHG spectrum from bulk diamond induced by an intense femtosecond laser pulse. Our result describes the intense HHG extending from the perturbative to highly non-perturbative incident laser intensity regimes. The non-perturbative regime of HHG occurs for laser intensity $I \geq 1 \text{ TW/cm}^2$. We find that the HHG spectra from diamond exhibit two plateaus, the second plateau extending beyond the limit of the corresponding gas-phase harmonics emitted for the same laser intensity. We find that HHG and cutoff law are sensitive to details of the substrate band structure involving strong interband couplings between multiple single-particle states. The numerical results make evident the feasibility of diamond for sub-femtosecond pulse generation.

-
- [1] J. Isberg, J. Hammersberg, E. Johansson, T. Wikström, D. J. Twitchen, A. J. Whitehead, S. E. Coe, and G. A. Scarsbrook, *Science* **297**, 1670 (2002).
 - [2] S. Lagomarsino, M. Bellini, C. Corsi, F. Gorelli, G. Parrini, M. Santoro, and S. Sciortino, Three-dimensional diamond detectors: Charge collection efficiency of graphitic electrodes, *Appl. Phys. Lett.* 103 (2013) 233507 ; doi: 10.1063/1.4839555.
 - [3] G. Conte, P. Allegrini, M. Pacilli, S. Salvatori, T. Kononenko, A. Bolshakov , V. Ralchenko, V. Konov, Three-dimensional graphite electrodes in CVD single crystal diamond detectors: Charge collection dependence on impinging beta-particles geometry, *Nucl. Instr. Meth A* 799 (2015) 10-16;doi:10.1016/j.nima.2015.07.024.
 - [4] F. Bachmair, L. Bä ni, P. Bergonzo, B. Caylar, G. Forcolin, I. Haughton, D. Hits, H. Kagan, R. Kass, L. Lie, A. Oh, S. Phan, M. Pomorski, D.S. Smith, V. Tyzhnevyyi, R. Wallny, D. Whitehead, A 3D Diamond Detector for Particle Tracking, *Nucl. Instr. Meth. A* 786 (2015) 97-104; doi: 10.1016/j.nima.2015.03.033
 - [5] I. Aharonovich and E. Neu, *Advanced Optical Materials* **2**, 911 (2014).

- [6] B. J. M. Hausmann, B. Shields, Q. Quan, P. Maletinsky, M. McCutcheon, J. T. Choy, T. M. Babinec, A. Kubanek, A. Yacoby, M. D. Lukin, and M. Loncar, *Nano Letters* **12**, 1578 (2012).
- [7] A. I. Kuznetsov, A. E. Miroshnichenko, M. L. Brongersma, Y. S. Kivshar, and B. Lukyanchuk, *Science*, **354**, 2472 (2016).
- [8] A. M. Ozkan, A. P. Malshe, T. A. Railkar, W. D. Brown, M. D. Shirk and P. A. Molian, *Appl. Phys. Lett.* **75**, 3716 (1999).
- [9] M. H. Pham, D. V. Pham, T. H. Do, A. K. Ivanova, A. A. Ionin, S. I. Kudryashov, A. O. Levchenko, L. Nguyen, T. T. H. Nguyen, A. A. Rudenko, I. N. Saraeva, *Communications in Physics* **26** (2016).
- [10] A. K. Ivanova, A. A. Ionin, R. A. Khmel'nitskii, S. I. Kudryashov, A. O. Levchenko, N. N. Mel'nik, A. A. Rudenko, I. N. Saraeva, S. P. Umanskaya, D. A. Zayarny, *Laser Physics Letters* (2016). (submitted)
- [11] A. Boltasseva and H. A. Atwater *Science* **331**, 290 (2011).
- [12] M. Z. Alam, I. De Leon, R. W. Boyd, *Science* **352**, 795 (2016).
- [13] S. Jahani, Z. Jacob, *Nature Nanotechnology*, **11**, 23 (2016).
- [14] P. R. West, S. Ishii, G. V. Naik, N. K. Emani, V. M. Shalaev, and A. Boltasseva, *Laser Photonics Rev.* **4**, 795 (2010).
- [15] G. V. Naik, V. M. Shalaev, A. Boltasseva, *Adv. Mater.* **25**, 3264 (2013).
- [16] S. Ghimire et al, *Nature Physics* **3**, 381 (2011)
- [17] G. Ndabashimiye, S. Ghimire, M. Wu, D. A. Browne, K. J. Schafer, M. B. Gaarde and D. A. Reis, *Nature* **522**, 462 (2016), doi:10.1038/nature17660
- [18] T. T. Luu, M. Garg, S. Y. Kruchinin, A. Moulet, M. T. Hassan, and E. Goulielmakis, *Nature (London)* **521**, 498 (2015)
- [19] T. Otake, *PHYSICAL REVIEW B* **94**, 235152 (2016)
- [20] N. Tancogne-Dejean, O. D. Mücke, F. X. Kartner, and A. Rubio, *PRL* **118**, 087403 (2017)
- [21] S. Lagomarsino, M. Bellini, C. Corsi, S. Fanetti, F. Gorelli, I. Liotos, G. Parrini, M. Santoro, S. Sciortino, Electrical and Raman-imaging characterization of laser-made electrodes for 3D diamond detectors, *Diamond Relat. Mater.* **43** (2014) 23-28.
- [22] Stefano Lagomarsino, Marco Bellini, Chiara Corsi, Vladimir Cindro, Keida Kanxheri, Arianna Morozzi, Daniele Passeri, Leonello Servoli, Christian J. Schmidt and Silvio Sciortino, Radiation hardness of three-dimensional polycrystalline diamond detectors, *Appl. Phys. Lett.* **106** (2015) 193509; doi: 10.1063/1.4921116.
- [23] H. O. Jeschke, M. E. Garcia, and K. H. Bennemann, Microscopic analysis of the laser-induced femtosecond graphitization of diamond, *Phys. Rev. B* **60**, R3701(R) (1999).
- [24] H. O. Jeschke, M. E. Garcia, K. H. Bennemann, Theory for laser-induced ultrafast phase transitions in carbon, *Appl. Phys. A* **69** [Suppl.], S49-S53 (1999).
- [25] D. M. Rayner, A. Naumov and P. B. Corkum, Ultrashort pulse non-linear optical absorption in transparent media, *Opt. Exp.* **13** (2005) 3208-3217.
- [26] T. Apostolova and Y. Hahn, *J. Appl. Phys.* **88**, 1024 (2000).
- [27] A. Kaiser, B. Rethfeld, M. Vicanek and G. Simon, *Phys. Rev. B* **61**, 11437 (2000).
- [28] M. Lenzner, J. Krüger, S. Sartania, Z. Cheng, Ch. Spielmann, G. Mourou, W. Kautek, and F. Krausz, *Phys. Rev. Lett.* **80**, 4076 (1998)

- [29] P. P. Rajeev, M. Gertszov, P. B. Corkum, and D. M. Rayner, *Phys. Rev. Lett.* **102**, 083001 (2009).
- [30] M. Hohenleutner, F. Langer, O. Schubert, M. Knorr, U. Huttner, S. W. Koch, M. Kira and R. Huber, *Nature* **523**, 572 (2015).
- [31] W. Slaslow, T. K. Bergstresser and M. Cohen, *Phys. Rev. Lett.* **16**, 354 (1966).
- [32] G. Pennigton and N. Goldsman, *Phys. Rev. B* **64**, 045104(2001)
- [33] J. B. Krieger and G. J. Iafrate, *Phys. Rev. B* **33**, 5494 (1986)
- [34] L. V. Keldysh, *Sov. Phys.-JETP* **20**, 1307 (1965).
- [35] I. Franco, M. Shapiro, and P. Brumer, *Phys. Rev. Lett.* **99**, 126802
- [36] C. Mézel, G. Duchateau, G. Geneste
- [37] V. E. Gruzdev, *Phys. Rev. B* **75**, 205106 (2007).
- [38] P. G. Hawkins and M. Yu. Ivanov, *Phys. Rev. A* **87**, 063842
- [39] T. Otake, M. Yamagiwa, J.-I. Iwata, K. Yabana, T. Nakatsukasa
- [40] A. Schiffrin, T. P.-Colberg, N. Karpowicz, V. Apalkov, D. Gerster
- [41] R. A. Smith. *Semiconductors*. 2nd ed. (Cambridge University,
- [42] L. S. Pan, D. R. Kania. *Diamond: electronics properties and applications*. The Kluwer International Series in Engineering and Computer Science. Kluwer Academic Publishers (1995), p.248
- [43] G. Miyaji and K. Miyazaki, *Optics Express* **16**, 16265 (2008).
- [44] M. Shinoda, R. R. Gattass and E. Mazur, *J. Appl. Phys.* **105**, 053102 (2009).
- [45] Q. Wu, Y. Ma, R. Fang, Y. Liao, and Q. Yu, *Appl. Phys. Lett.* **82**, 1703 (2003).
- [46] P. Calvani, A. Bellucci, M. Girolami, S. Orlando, V. Valentini, A. Lettino, & D. M. Trucchi, *Applied Physics A* **117**, 25 (2014).
- [47] J.E. Sipe, J.F. Young, J.S. Preston, H.M. van Driel, *Phys. Rev. B* **214**, 1141 (1983).
- [48] S.A. Akhmanov, V.I. Emelyanov, N.I. Koroteev, V.N. Seminogov, *Sov. Phys. Usp.* **28**, 1084 (1985).
- [49] M. Huang, F. Zhao, Y. Cheng, N. Xu, and Z. Xu, *Phys. Rev. B*, **79**, 125436 (2009).
- [50] O. Varlamova, J. Reif, S. Varlamov and M. Bestehorn, *Appl. Surf. Sci.* **252**, 4702 (2006).
- [51] G. Tsibidis, M. Barberoglou, P. Loukakos, E. Stratakis, and C. Fotakis. *Phys. Rev. B* **86**, 115316 (2012).
- [52] M. Huang, F. Zhao, Y. Cheng, N. Xu, and Z. Xu, *ACS Nano* **3**, 4062 (2009).
- [53] J. Bonse, J. Krüger, *J. Appl. Phys.* **108**, 034903 (2010).
- [54] G. D. Tsibidis, E. Skoulas, E. Stratakis, *Opt. Lett.* **40**, 5172 (2015).
- [55] P.A. Danilov, A.A. Ionin, S.I. Kudryashov, S.V. Makarov, A.A. Rudenko, P.N. Saltuganov, L.V. Seleznev, V.I. Yurovskikh, D.A. Zayarny, T. Apostolova, *J. Exp.Theor. Phys.* **120**, 946 (2015).
- [56] A.A. Ionin, S.I. Kudryashov, S.V.Makarov, L.V. Seleznev, and D.V. Sinitsyn, *Laser Physics Letters* **12**, 025902 (2015).
- [57] A.A. Ionin, S.I. Kudryashov, L.V. Seleznev, D.V. Sinitsyn, V.I. Emel'yanov, *JETP Lett.* **97**, 121, (2013).
- [58] A. Borowiec and H. K. Hagen, *Appl. Phys. Lett.* **82**, 4462 (2003).
- [59] E.V. Golosov, A.A. Ionin, Yu.R. Kolobov, S.I. Kudryashov, A. E. Ligachev, S.V. Makarov, Yu.N. Novoselov, L.V. Seleznev, D.V. Sinitsyn, A.R. Sharipov, *Phys. Rev. B* **83**, 115426 (2011).
- [60] C.S.R. Nathala, A. Ajami, A.A. Ionin, S.I. Kudryashov, S.V. Makarov, T. Ganz, A. Assion, W. Husinsky, *Optics Express* **23**, 5915 (2015).

- [61] H. M. van Driel, J. E. Sipe, and J. F. Young, *Phys. Rev. Lett.* **49**, 1955 (1982).
- [62] J. Bonse, M. Munz and H. Sturm, *J. Appl. Phys.* **97**, 013538 (2005).
- [63] T. Q. Jia, H. X. Chen, M. Huang, F. L. Zhao, J. R. Qiu, R. X. Li, Z. Z. Xu, X. K. He, J. Zhang, and H. Kuroda, *Phys. Rev. B* **72**, 125429 (2005).
- [64] D. Dufft, A. Rosenfeld, S. K. Das, R. Grunwald, and J. Bonse, *J. Appl. Phys.* **105**, 034908 (2009).
- [65] P. C. Becker, H. L. Fragnito, C. H. Brito Cruz, R. L. Fork, J. E. Cunningham, J. E. Henry, and C. V. Shank, *Phys. Rev. Lett.* **61**, 1647 (1988).
- [66] Y. Shimotsuma, P. G. Kazansky, J. Qiu, and K. Hirao, *Phys. Rev. Lett.* **91**, 247405 (2003).
- [67] J. Bonse, A. Rosenfeld, and J. Krger, *J. Appl. Phys.*, **106**, 104910 (2009).
- [68] B. H. Christensen and P. Balling, *Phys. Rev. B* **79**, 155424 (2009).
- [69] D. H. Reitze, , H. Ahn and M. C. Downer, *Phys. Rev. B* **45**, 2677 (1992).
- [70] K. Sokolowski-Tinten, D. von der Linde, *Phys. Rev. B* **61**, 2643 (2000).
- [71] S. A. Sato, K. Yabana, Y. Shinohara, T. Otobe, and G. F. Bertsch *Phys. Rev. B* **89**, 064304 (2014).
- [72] S. A. Sato, K. Yabana, Y. Shinohara, T. Otobe and G. F. Bertsch, *Phys. Rev. B* **92**, 205413 (2015).
- [73] J. Z. P. Skolski, G. R. B. E. Römer, J. V. Obona, V. Ocelik, A. J. Huis in't Veld, and J. Th. M. De Hosson, *Phys. Rev. B* **85**, 075320 (2012).
- [74] S. Lagomarsino, S. Sciortino, B. Obreshkov, T. Apostolova, C. Corsi, M. Bellini, E. Berdermann, and C. J. Schmidt, *Phys. Rev. B* **93**, 085128 (2016).
- [75] E.J. Yoffa, *Phys. Rev. B* **21**, 2415 (1980).
- [76] W. S. Fann, R. Storz, H. W. K. Tom, and J. Bokor, *Phys. Rev. B* **46**, 13592 (1992).
- [77] T. Apostolova and Y. Hahn, *J. Appl. Phys.* **88**, 1024 (2000).
- [78] B. C. Stewart, M. D. Feit, S. Herman, A. M. Rubenchik, B. W. Shore, and M. D. Perry, *Phys. Rev. B* **53**, 11449 (1995).
- [79] T. Watanabe, T. Teraji, T. Ito, Y. Kamakura, and K. Taniguchi, *Appl. J. Phys.* **95**, 4866 (2004).
- [80] R.H.M. Groeneveld, R. Sprik, A. Lagendijk, *Phys. Rev. B* **51**, 11433 (1995).
- [81] K. El-Sayed in "Microscopic Theory of Semiconductors Quantum Kinetics, Confinement and Lasers", Edited by: S. W. Koch, World Scientific, (1995)
- [82] P. Danilov, D. Zayarny, A.A. Ionin, S.I. Kudryashov, T.H. Nguyen, .. Rudenko, I.N. Saraeva, .. Kuchmizhak, .B. Vitrik, Yu.N. Kulchin, *JETP Lett.* **103** , 549 (2016)
- [83] X. Jia, T. Q. Jia, N. N. Peng, D. H. Feng, S. A. Zhang, and Z. R. Sun, *J. Appl. Phys.* **115**, 143102 (2014).
- [84] A. McPherson, G. Gibson, H. Jara, U. Johann, T. S. Luk, I. A. McIntyre, K. Boyer, and C. K. Rhodes, *J. Opt. Soc. of Am. B* **4**, 595-601 (1987).
- [85] M. Ferray, A. L'Huillier, X. F. Li, L. A. Lompre, G. Mainfray and C. Manus, *J. Phys. B: At. Mol. Opt. Phys.* **21** L31, (1988).
- [86] K. C. Kulander, K. J. Schafer, J. L. Krause, *Super-Intense Laser-Atom Physics*. Ed. B. Piraux, A. L'Huillier, and K. Rzazewski. D. Reidel Publishing Company, Dordrecht-Holland. NATO Advanced Study Institutes Series. B **316**, 95 (1993).
- [87] A. L'Huillier and P. Balcou, *Phys. Rev. Lett.* **70**, 774 (1993)
- [88] J. J. Macklin, J. D. Kmetec, and C. L. Gordon, *Phys. Rev. Lett.* **70**, 766 (1993)

- [89] U. Teubner and P. Gibbon, *Rev. Mod. Phys.* **81**, 445 (2009)
- [90] M. Abd-Elmeguid et al., *Tesla Technical Design Report, The X-ray Free Electron Laser (DESY, Hamburg, 2001)*
- [91] H. Winick Ed., *Synchrotron Radiation Sources*, World Scientific Pub. Co. Inc., World Scientific Series on Synchrotron Radiation Techniques(1995).
- [92] G. Farkas and C. Toth, *Phys. Lett. A* 168, 447 (1992)
- [93] P. B. Corkum and F. Krausz, *Attosecond Science, Nat. Phys.*, 3, 381, (2007)
- [94] F. Krausz and M. Ivanov, *Rev. Mod. Phys.* 81, 163 (2009)
- [95] Martin Schultze, Krupa Ramasesha, C.D. Pemmaraju, S.A. Sato, D. Whitmore, A. Gandman, James S. Prell, L. J. Borja, D. Prendergast, K. Yabana, Daniel M. Neumark, Stephen R. Leone, *Science* 12 Dec 2014: Vol. 346, Issue 6215, pp. 1348-1352, DOI: 10.1126/science.1260311
- [96] N. H. Chapman, P. Fromme, A. Barty et al, *Femtosecond X-ray protein nanocrystalography*, *Nature* 470, 73, 2011
- [97] O. D. Mucke, *Phys. Rev. B* 84, 081202 (2011).
- [98] S. Ghimire, A. D. DiChiara, E. Sistrunk, G. Ndabashimiye, U. B. Szafruga, A.Mohammad, P. Agostini, L. F. DiMauro, and D. A. Reis, *Phys. Rev. A* 85, 043836 (2012).
- [99] G. Vampa, C. R. McDonald, G. Orlando, D. D. Klug, P. B. Corkum, and T. Brabec, *Phys. Rev. Lett.* **113**, 073901 (2014).
- [100] T. Higuchi, M. I. Stockman, and P. Hommelhoff, *Phys. Rev. Lett.* **113**, 213901, (2014).
- [101] O. Schubert, M.Hohenleutner, F. Langer, B. Urbanek, C. Lange, U. Huttner, D. Golde, T. Meier, M. Kira, S. W. Koch, and R. Huber, *Nat. Photonics* 8, 119 (2014).
- [102] T. Otobe, *Journal of Applied Physics* 111, 093112 (2012), T. Otobe, K. Yabana, and J.-I. Iwata, *Journal of Computational and Theoretical Nanoscience*, 6, 2545, 2009
- [103] T. Otobe, *Journal of Applied Physics* 111, 093112 (2012)
- [104] T. T. Luu and H. J. Weorner *Phys. Rev. B* 94, 115164 (2016)
- [105] G. Vampa, C. R. McDonald, G. Orlando, P. B. Corkum, and T. Brabec, *Phys. Rev. B* **91**, 064302 (2015)
- [106] X. Chu, S-I. Chu, C. Laughlin, *Phys. Rev. A* **64**, 013406 (2001)

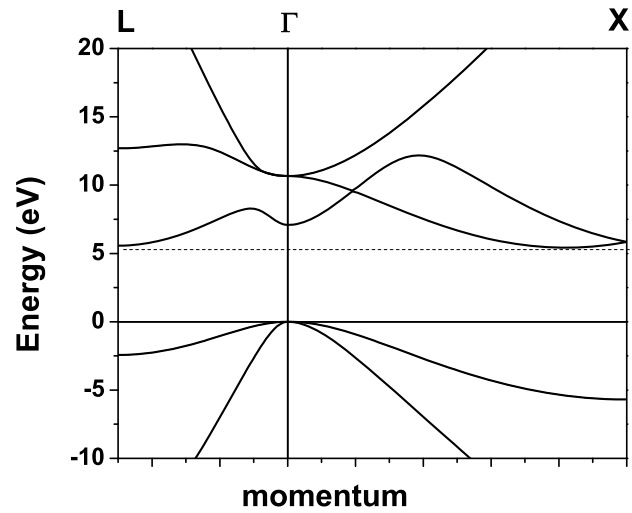


FIG. 1. Static band structure of diamond along the ΓX and ΓL directions in the Brillouin zone. The crystal momentum is given in units of $2\pi/a_0$.

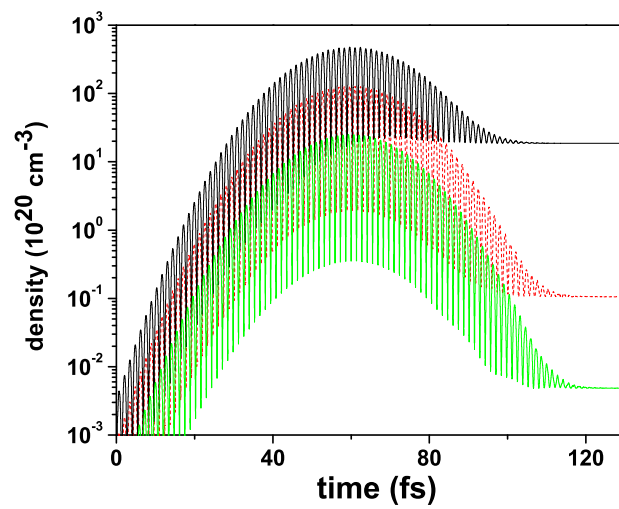


FIG. 2. Time-evolution of the electron density for three different peak intensities of 30fs laser pulse interacting with diamond. $I = 1.5 \text{ TW/cm}^2$ (dotted line), $I = 10 \text{ TW/cm}^2$ (dashed line) and $I = 50 \text{ TW/cm}^2$ (solid line).

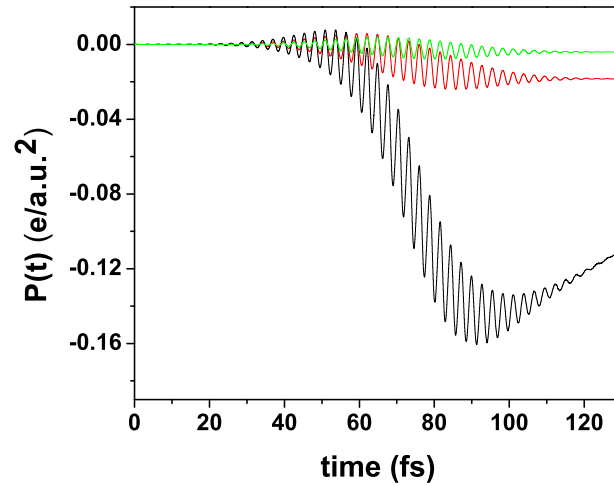


FIG. 3. Time-evolution of the macroscopic polarization density along the laser polarization direction for three different peak intensities of 30fs laser pulse interacting with diamond. $I = 1.5 \text{ TW/cm}^2$ (green line), $I = 10 \text{ TW/cm}^2$ (red line) and $I = 50 \text{ TW/cm}^2$ (black line).

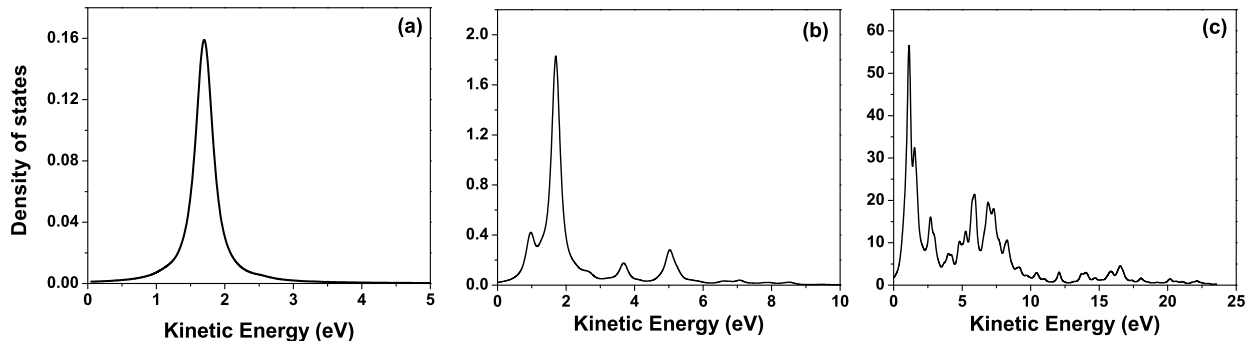


FIG. 4. Density of conduction band states after the irradiation of diamond with 30fs laser pulse linearly polarized parallel to bonds between carbon atoms. In Fig.(a) the peak intensity of the light pulse is $I = 1.5 \text{ TW/cm}^2$. In Fig.(b) and (c) the peak intensity is $I = 10 \text{ TW/cm}^2$ and $I = 50 \text{ TW/cm}^2$, respectively. The kinetic energy of the released electrons is measured relative to the conduction band minimum.

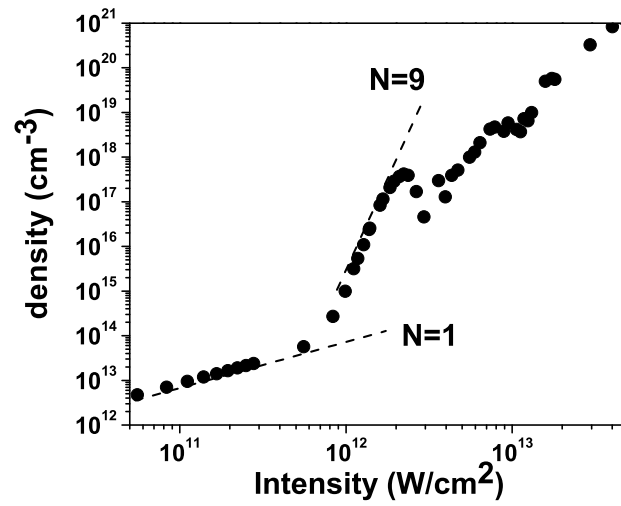


FIG. 5. Intensity dependence of the photoionization yield after the irradiation of diamond with 30fs laser pulse linearly polarized parallel to bonds between carbon atoms.

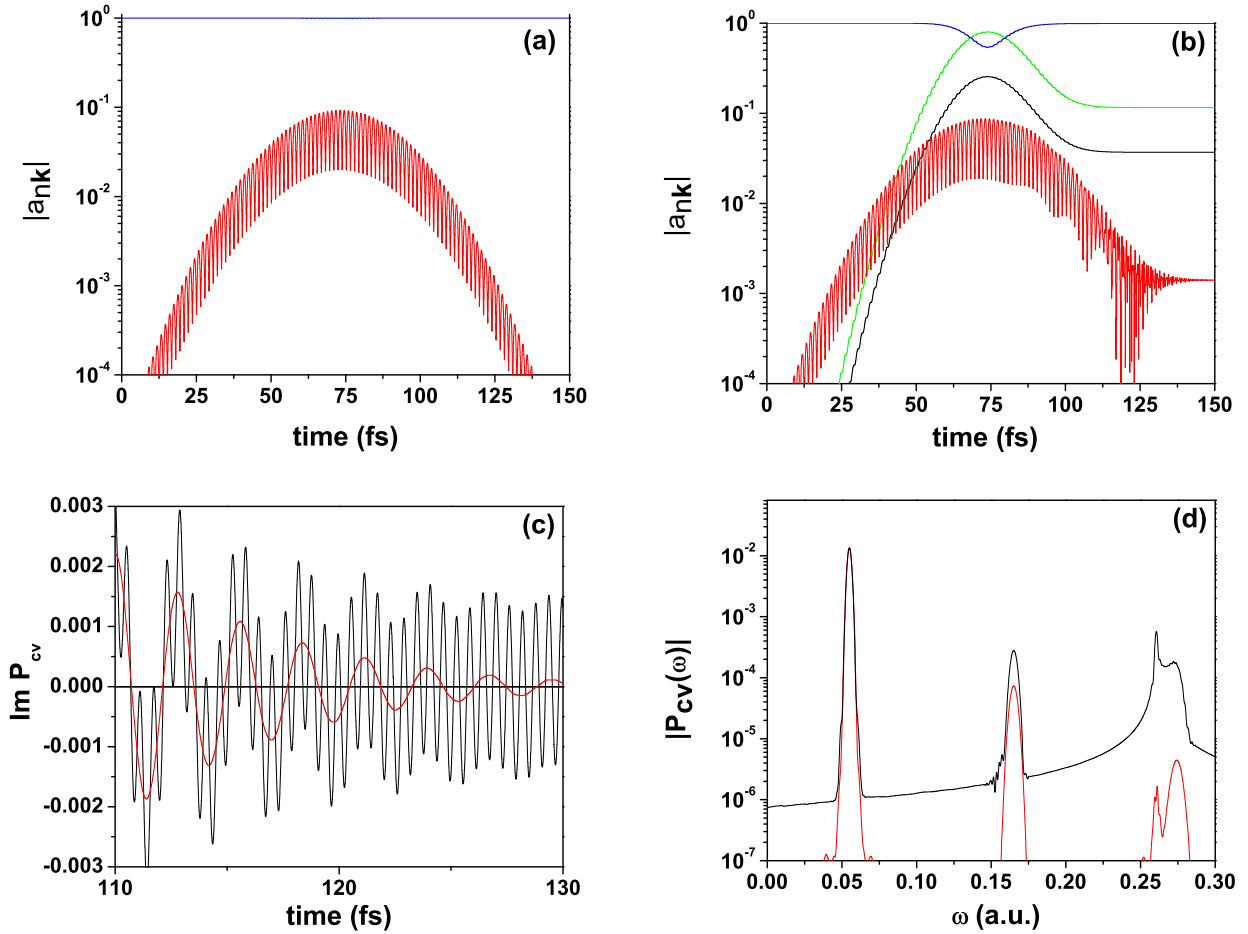


FIG. 6. Perturbative vs. non-perturbative multiphoton ionization of diamond interacting with 30fs laser pulse with intensity = 1.5 TW/cm^2 . Fig. (a) Time evolution of the modulus of the Fourier amplitudes $|a_{nk}|$ in the expansion of the photoelectron wave-packet over Bloch states with $\mathbf{k} = (0, 0, 0)$ by neglecting laser-induced interactions among valence bands (cf. also text). Valence and conduction band amplitudes are given by blue and red lines, respectively. Fig.(b) shows the time evolution of the modulus of the Fourier amplitudes by including laser-induced dipole-dipole interactions between the three valence bands at the Brillouin zone centre (blue, green and black lines), the photoionization amplitude is given by the red line. Fig.(c) shows the imaginary part of the interband polarization by neglecting (red curve) and by including indirect photoionization pathways (black curve) and Fig.(d) gives the frequency-dependence of the modulus of the Fourier transform of the interband polarization.

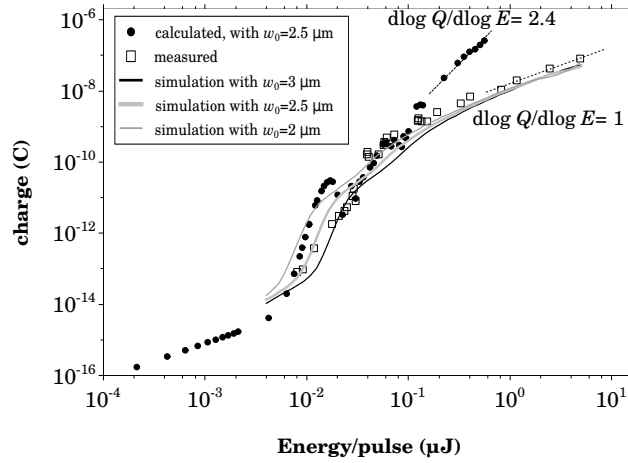


FIG. 7. Comparison of theory and data. Square markers: generated charge as a function of the pulse energy from experimental data. Circles: generated charge derived from the theoretical electron yield in Fig. 5 distributed in an effective ellipsoidal volume of axis $w_0 = 2.5 \mu\text{m}$ and $z_R = 35 \mu\text{m}$. Black, gray and light gray lines: charge calculated from Eq. 15 as a function of the pulse energy calculated with Eq. 15 for $w_0=2, 2.5$ and $3 \mu\text{m}$.

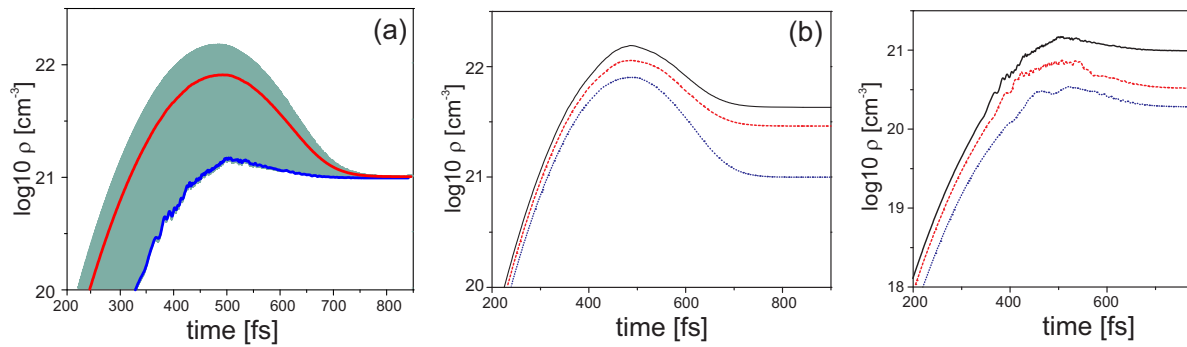


FIG. 8. Time evolution of the free-electron density in diamond irradiated by 200fs laser pulse with intensity 30 TW/cm^2 , linearly polarized along the (1,1,1) direction. The red curve shows the cycle-averaged electron density and the blue curve is the electron density. (b) The cycle-averaged carrier densities for intensity $I=30, 40$ and 50 TW/cm^2 are shown by the dashed-dotted, dashed and solid lines, respectively. The position of the pulse peak is indicated by the vertical dashed line and Fig. (c) presents the number density of non-adiabatically excited carriers for intensity $I=30, 40$ and 50 TW/cm^2

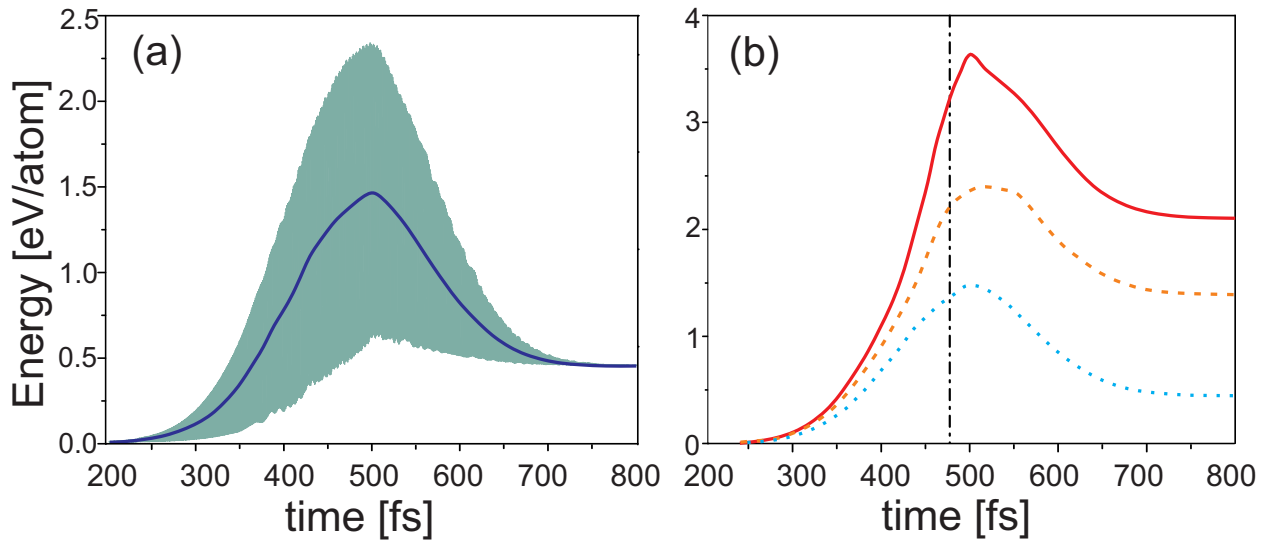


FIG. 9. (a) Instantaneous excitation energy of electrons interacting with 200fs laser pulse with intensity 30 TW/cm^2 (linearly polarized along the (1,1,1) direction), the green curve shows the cycle-averaged electronic excitation energy. (b) The cycle-averaged excitation energy for laser intensity $I=30, 40$ and 50 TW/cm^2 is shown by the dashed-dotted, dashed and solid lines, respectively. The position of the pulse peak is indicated by the vertical dashed line.

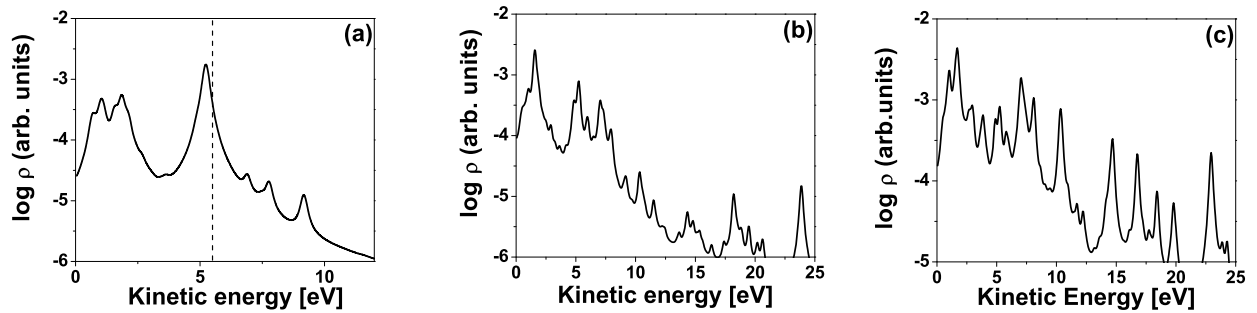


FIG. 10. Density of conduction states after the irradiation of bulk diamond with 200fs laser pulse. The energy is measured relative to the conduction band minimum. The laser intensity is $I = 10, 20$ and 30 TW/cm^2 in Fig. (a-c), respectively. The vertical dashed line in Fig. a indicates the threshold for impact ionization

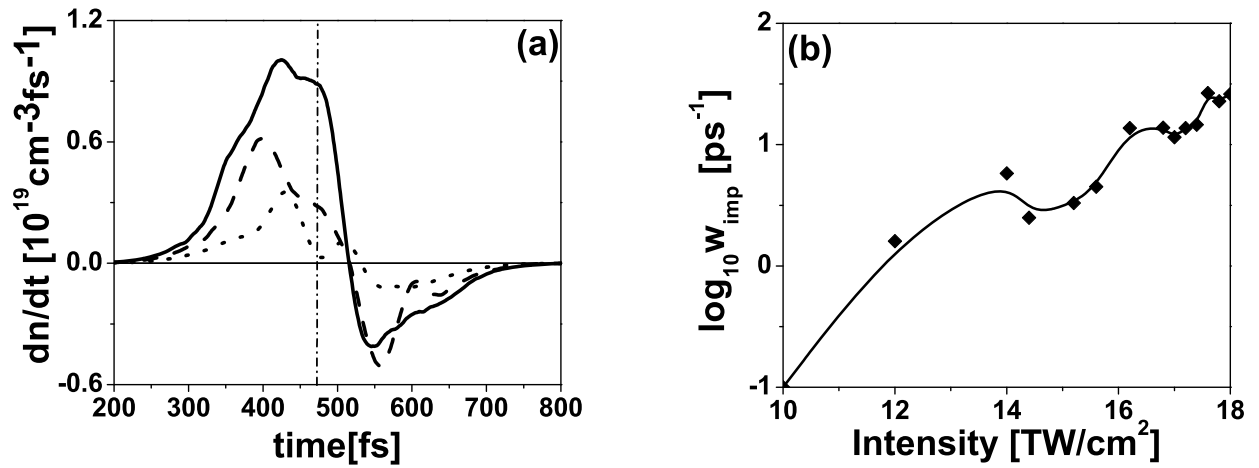


FIG. 11. Fig. (a) Time-dependent rates including carrier generation (positive part) and laser-induced recombination (negative part). The laser intensity is 10 TW/cm² (dotted), 20 TW/cm² (dashed) and 30 TW/cm² (solid line). Fig.(b) shows the intensity-dependent impact ionization rate.

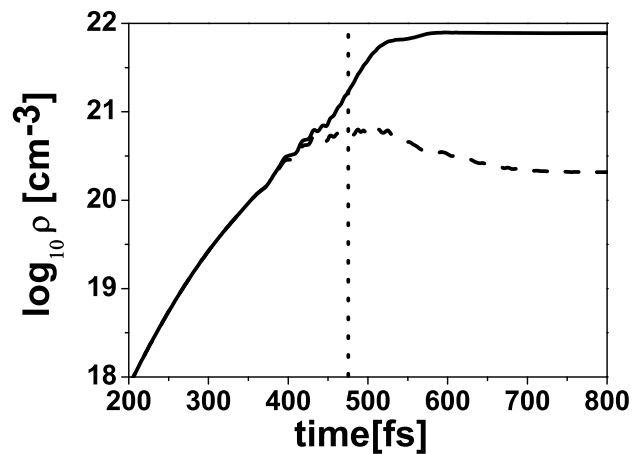


FIG. 12. Conduction electron density due to photoionization only (dashed line) and including the impact ionization (solid line). The laser intensity is 18 TW/cm². The vertical dotted line indicates the position of the pulse peak.

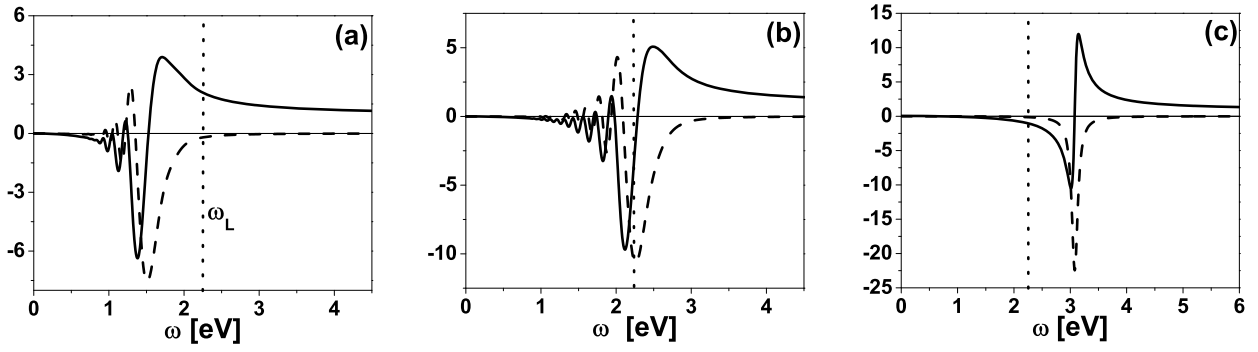


FIG. 13. Frequency dependence of the real (solid line) and imaginary part (dashed line) of the inverse dielectric function of photoexcited carriers subjected to 200 fs laser pulse with intensity 18 TW/cm². The time interval is measured relative to the peak of the pulse ($t = 0$). In Fig. (b) $t = 50$ fs, and in Fig. (c) $t = 250$ fs. The photon energy is indicated by the vertical dotted line.

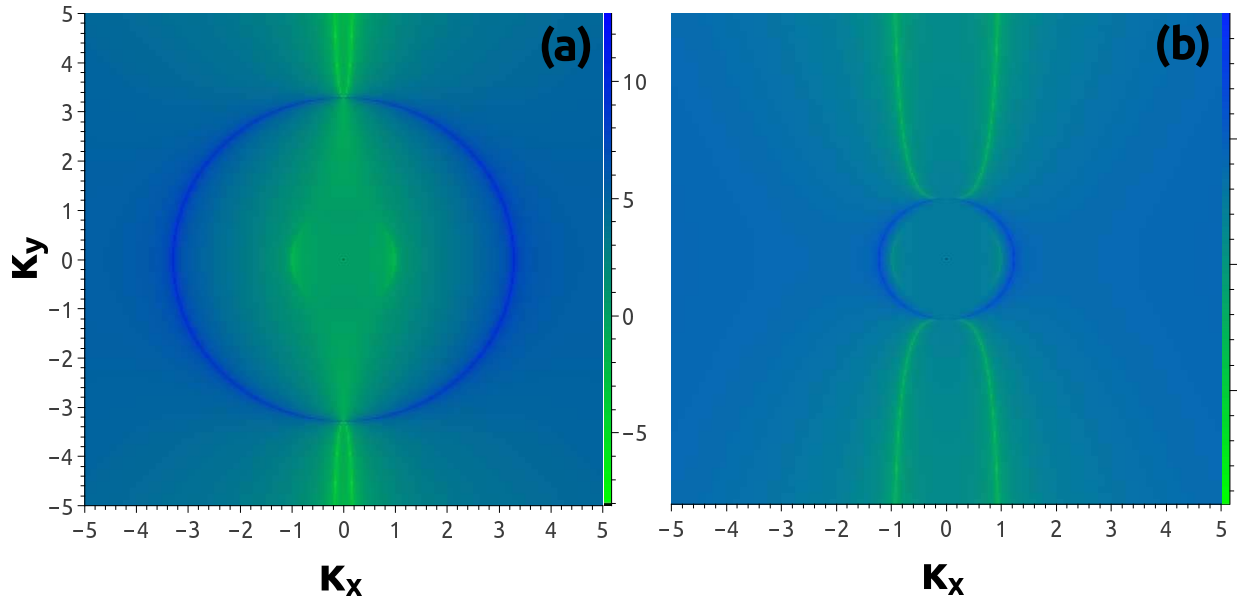


FIG. 14. 2D intensity map of the logarithm of the transient efficacy factor of laser-irradiated diamond, as a function of the normalized (to the laser wavelength) LIPSS wave vector components (κ_x, κ_y), for Instantaneous bulk plasma frequency (a) $\omega_p(t) = 1.5\omega_L$ and (b) $\omega_p(t) = 1.43\omega_L$. The laser beam is linearly polarized along the y-axis and is normally incident to the surface.

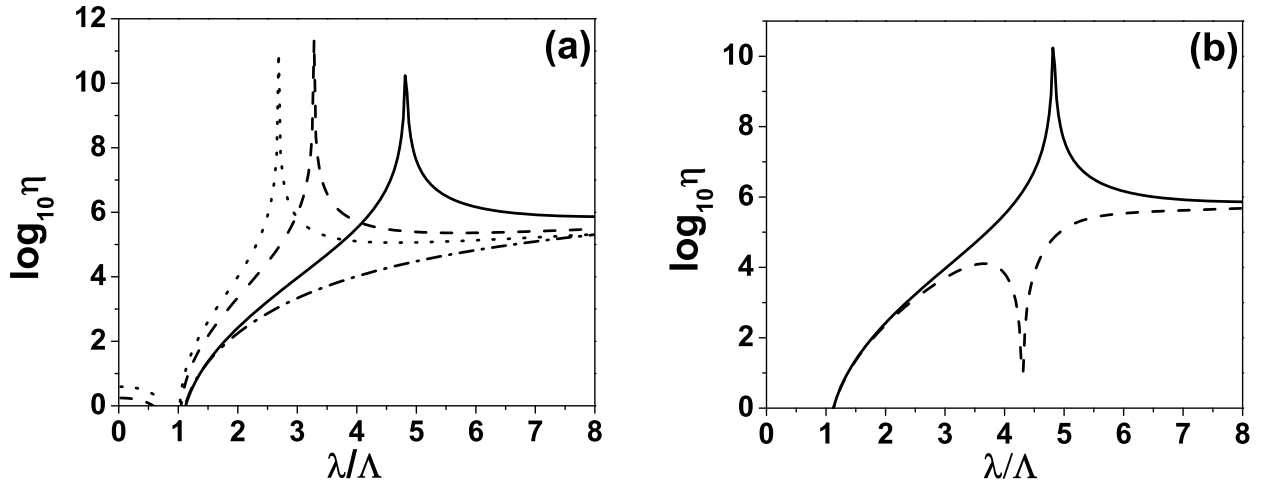


FIG. 15. Transient variation of the efficacy factor in the direction perpendicular to the laser polarization. In Fig. (a), the dashed-dotted line the EHP frequency $\omega_p(t) = 1.4\omega_L$ is just below the SPR excitation threshold, the solid line represents resonant excitation of surface plasmons corresponding to instantaneous bulk plasma frequency $\omega_p(t) = 1.43\omega_L$, the transient increase of the free-carrier density with $\omega_p(t) = 1.45\omega_L$ (dashed line) and $\omega_p(t) = 1.47\omega_L$ (dotted line) results in red-shift of the surface plasmon peak towards the light line and formation of near wavelength ripples. Fig.(b) demonstrates the dependence of the efficacy factor on the Drude damping time $\tau_e = 100$ fs (solid line) and $\tau_e = 10$ fs (dashed line). The laser beam is linearly polarized along the y -axis and is normally incident to the surface, λ and Λ designate the laser wavelength and the LIPSS period, respectively.

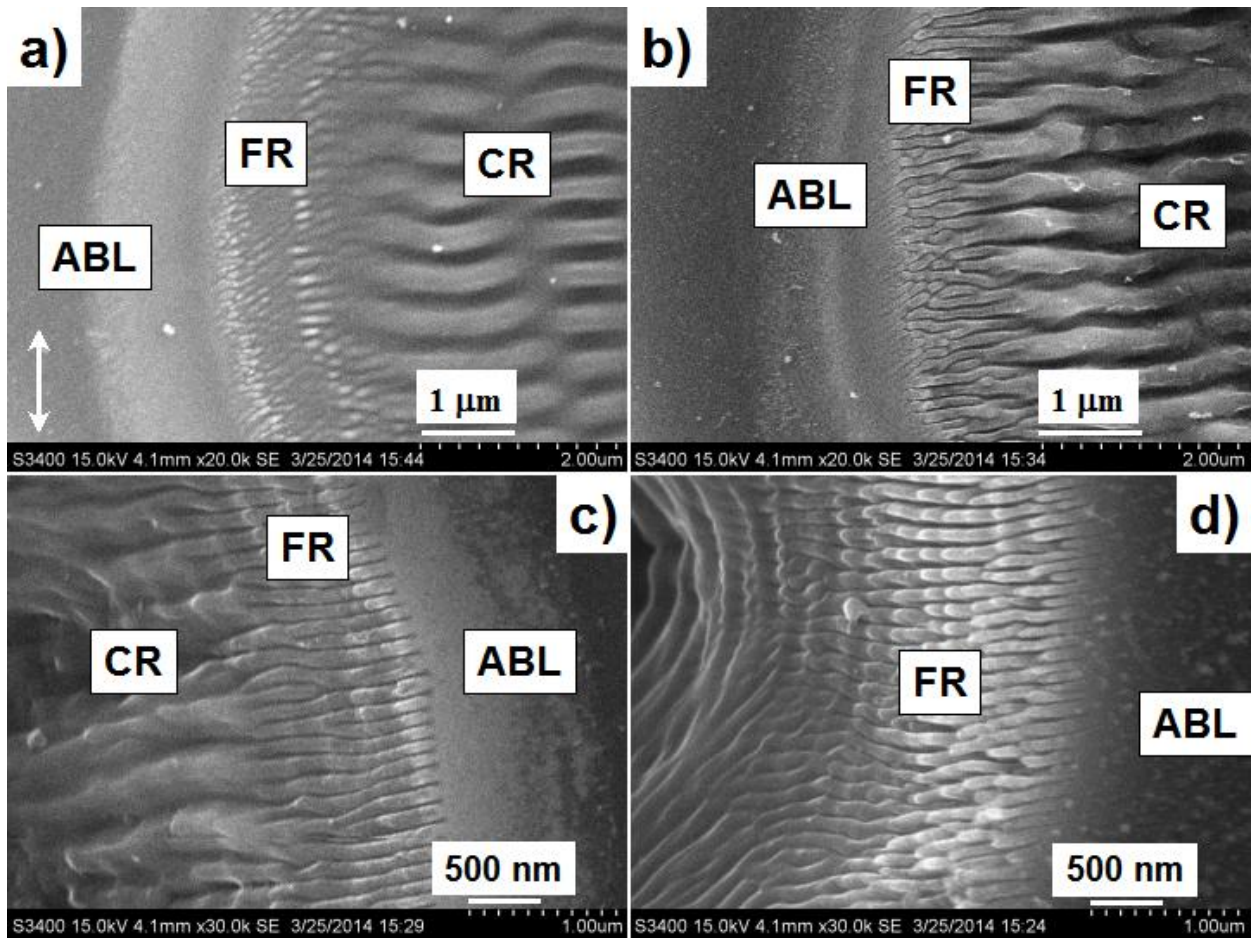


FIG. 16. SEM images of ablation crater edge (ABL), fine (FR) and coarse (CR) rippled regions within the craters on the diamond surface for $N = 10$ (a), 30 (b), 100 (c), and 300 (d) pulses. The scale bars are different on each image and the bi-lateral arrow in a) shows the laser polarization.

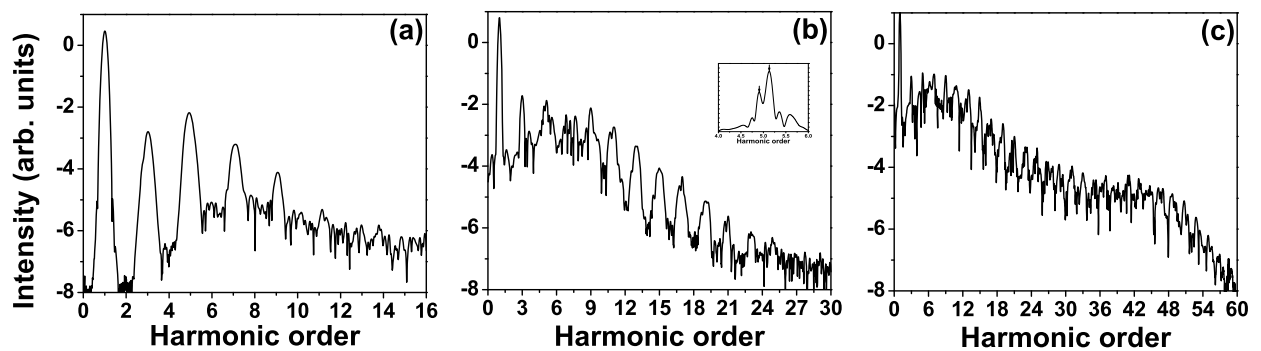


FIG. 17. HHG spectra obtained for photon energy 1.55 eV and pulse duration 15 fs. The intensity is 2, 10 and 30 TW/cm^2

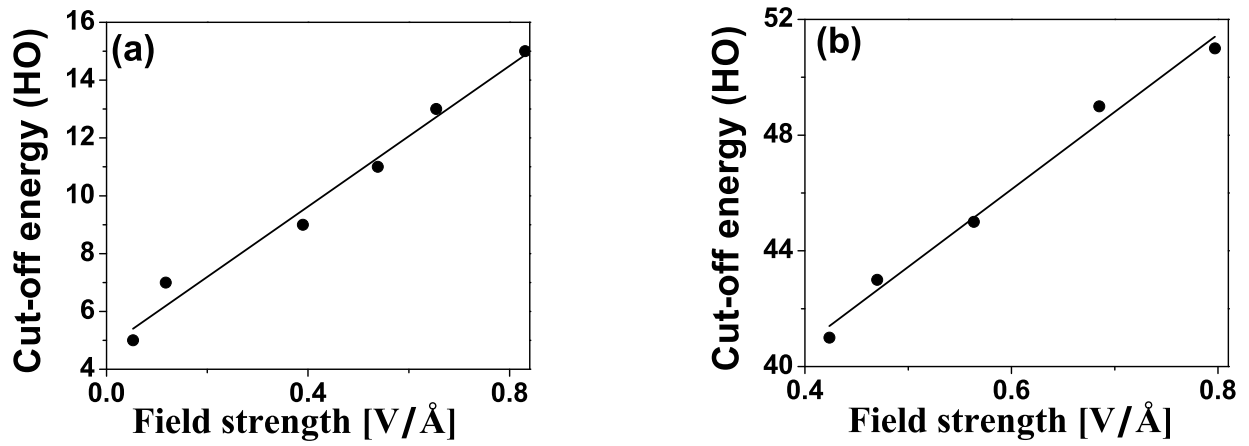


FIG. 18. High-energy cutoff as a function of the driving laser field for the first plateau (a) and the second plateau in (b)

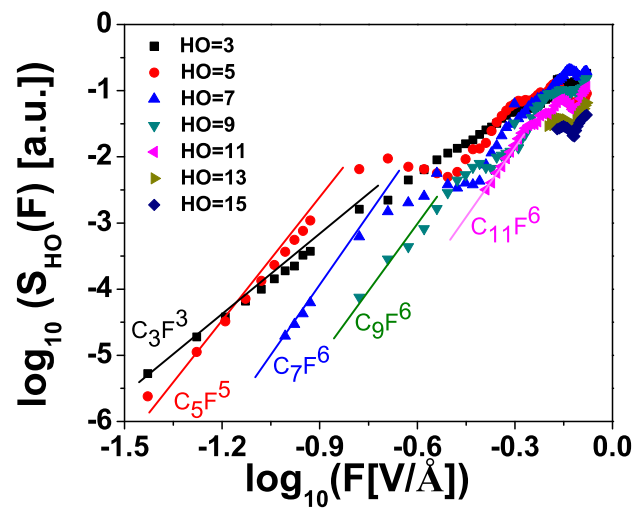


FIG. 19. Dependence of the spectral intensity of individual harmonics on the electric field strength

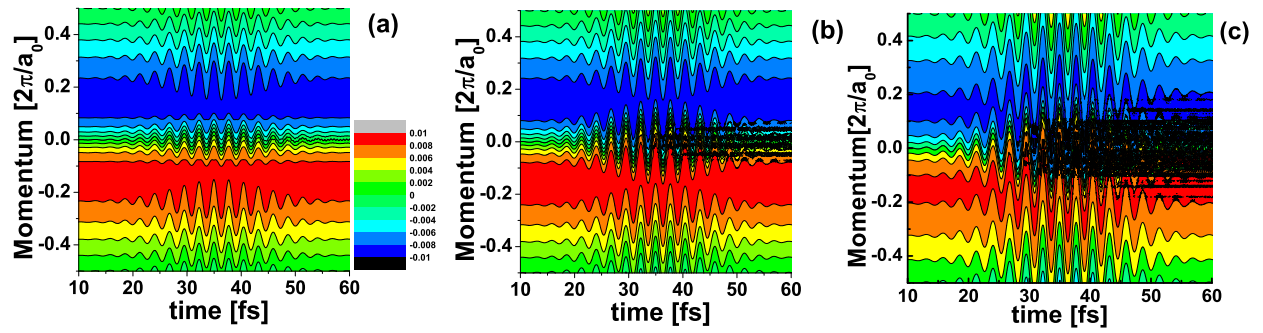


FIG. 20. Current density distribution in diamond bulk driven by intense 15fs laser pulse. The laser intensity is: (a) $I = 2\text{TW}/\text{cm}^2$, (b) $I = 10\text{TW}/\text{cm}^2$ and (c) $I = 30\text{TW}/\text{cm}^2$

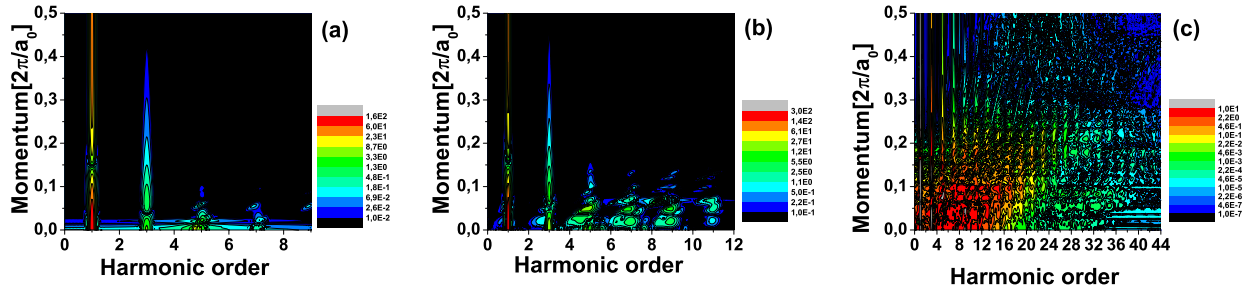


FIG. 21. Momentum-dependent HHG spectrum

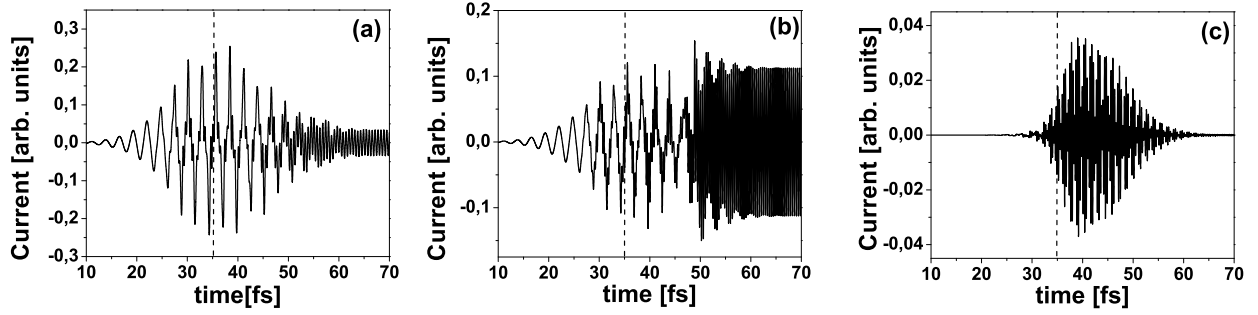


FIG. 22. Time evolution of the optically-induced polarization current corresponding to recombination of electrons with the light-hole band close to the BZ center. Fig. (a) 5-photon transition into the lowest conduction band ($n_c = 1$), Fig.(b) 7-photon transition into the first excited conduction band ($n_c = 2$). Fig.(c) presents the temporal profile of the current associated with the emission of 9th cutoff harmonic. In Fig. (a-c) the laser intensity is $I = 10 \text{ TW/cm}^2$ and the crystal momentum is $\mathbf{k} = \frac{2\pi}{a_0}(0.007, 0.007, 0.007)$, where a_0 is the bulk lattice constant.

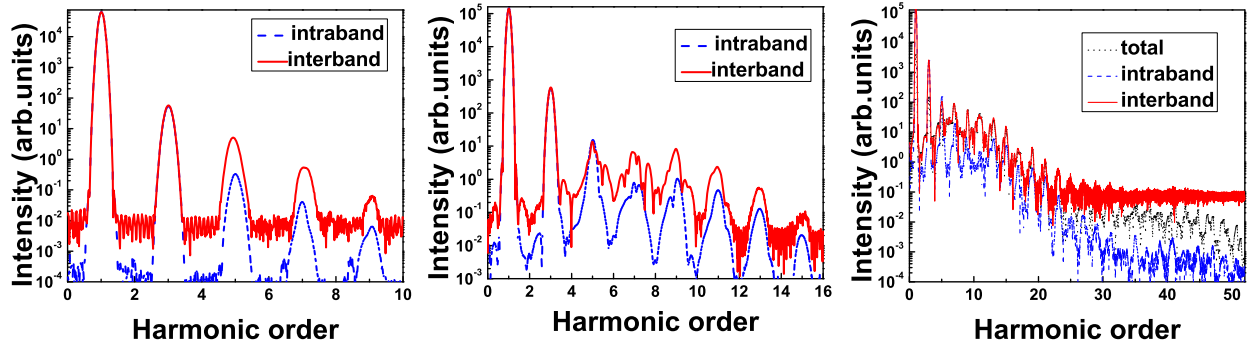


FIG. 23. Harmonic spectrum for interband (solid line), intraband (dashed line) and total (dotted line) currents

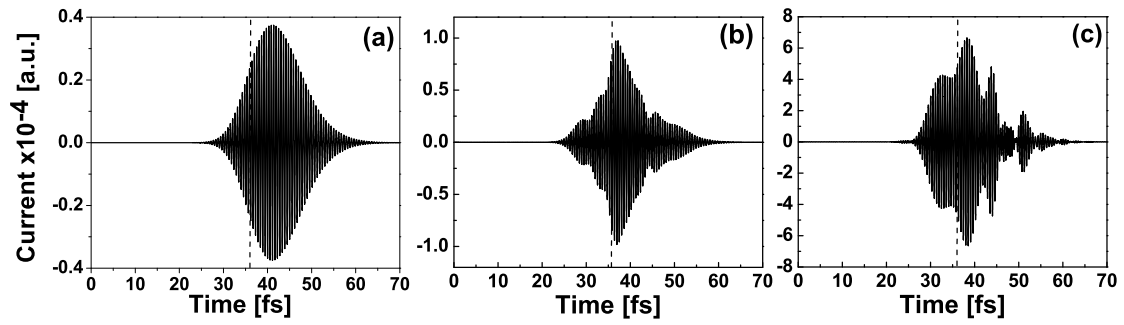


FIG. 24. The time-profile of the polarization current generating the 5th harmonic for the three different intensities - for three different laser intensities $I = 2, 10$ and 30 TW/cm^2

Symbols, Abbreviations, and Acronyms are explained in the text